

# Raman Line Imaging of Poly( $\epsilon$ -caprolactone)/Carbon Dioxide Solutions at High Pressures: A Combined Experimental and Computational Study for Interpreting Intermolecular Interactions and Free-Volume Effects

Maria Giovanna Pastore Carbone,<sup>†</sup> Pellegrino Musto,<sup>\*,‡</sup> Marianna Pannico,<sup>‡</sup> Andreas Braeuer,<sup>§</sup> Giuseppe Scherillo,<sup>†</sup> Giuseppe Mensitieri,<sup>†</sup> and Ernesto Di Maio<sup>†</sup>

<sup>†</sup>Department of Chemical, Materials and Production Engineering, University of Naples Federico II, P.le Tecchio 80, 80125 Naples, Italy

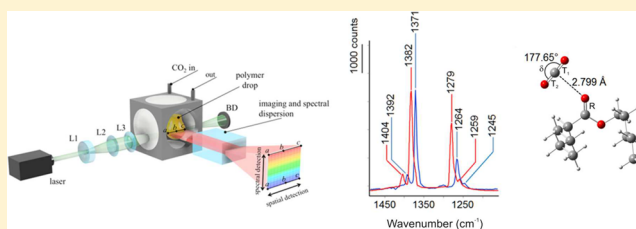
<sup>‡</sup>Institute on Polymers Composites and Biomaterials, National Research Council of Italy, 80078 Pozzuoli, Italy

<sup>§</sup>Erlangen Graduate School in Advanced Optical Technologies (SAOT) and Lehrstuhl für Technische Thermodynamik (LTT), Friedrich-Alexander-Universität Erlangen-Nürnberg, 91054 Erlangen, Germany

## S Supporting Information

**ABSTRACT:** In the present study, a Raman line-imaging setup was employed to monitor *in situ* the CO<sub>2</sub> sorption at elevated pressures (from 0.62 to 7.10 MPa) in molten PCL. The method allowed the quantitative measurement of gas concentration in both the *time-resolved* and the *space-resolved* modes. The combined experimental and theoretical approach allowed a molecular level characterization of the system. The dissolved CO<sub>2</sub> was found to occupy a volume essentially coincident with its van der Waals volume and the estimated

partial molar volume of the probe did not change with pressure. Lewis acid–Lewis base interactions with the PCL carbonyls was confirmed to be the main interaction mechanism. The geometry of the supramolecular complex and the preferential interaction site were controlled more by steric than electronic effects. On the basis of the indications emerging from Raman spectroscopy, an equation of state thermodynamic model for the PCL–CO<sub>2</sub> system, based upon a compressible lattice fluid theory endowed with specific interactions, has been tailored to account for the interaction types detected spectroscopically. The predictions of the thermodynamic model in terms of molar volume of solution have been compared with available volumetric measurements while predictions for CO<sub>2</sub> partial molar volume have been compared with the values estimated on the basis of Raman spectroscopy.



## INTRODUCTION

Poly( $\epsilon$ -caprolactone) (PCL) is a synthetic polyester which finds wide application in several technological fields and, in particular, in the biomedical sector. The reasons for its success are manifold: it is semicrystalline with a melting point above body temperature ( $T_m = 332$ – $337$  K), and a  $T_g$  of 213 K, which imparts toughness, being the amorphous phase in the rubbery state.<sup>1,2</sup> PCL is readily degraded by microorganisms and was proposed as a biodegradable packaging material. This application was limited by the sensible price of the polymer in comparison to competing materials. It was later recognized that hydrolytic degradation under physiological conditions was also feasible, albeit at a slower rate compared to natural biopolymers like poly(ethylene glycol) (PEG) and poly(lactic acid) (PLA)<sup>3</sup> because of the presence of five hydrophobic CH<sub>2</sub> moieties in the repeating unit. Applications have been proposed for PCL and PCL-based copolymers as delivery devices and commercial sutures.<sup>1,4,5</sup>

By far, the most successful application of PCL is in tissue engineering. In this area, it is employed as a matrix material to

realize scaffolds with designed microstructure. These provide structural support and controlled mass transport for the growing tissue, also serving as 3D template for cell adhesion, proliferation and differentiation. PCL and chemically modified PCL's, owing to their biocompatibility, tunable biodegradability, easy fabrication and adequate mechanical properties, have been used for a wide spectrum of scaffolds for skin, cartilage, bone, and cardiac constructs.<sup>6</sup> One of the most promising technologies for scaffold preparation is the CO<sub>2</sub>-foaming process, which can provide porous structures with carefully controlled morphology.<sup>7–9</sup> Among the attractive features of this processing technology, the most relevant is certainly its solvent-free, green-chemistry character. Gas-foaming is a complex process based on the nucleation and growth of gas bubbles (internal phase) dispersed throughout a polymer matrix (continuous phase) and its effective design

**Received:** March 8, 2016

**Revised:** July 25, 2016

**Published:** July 25, 2016

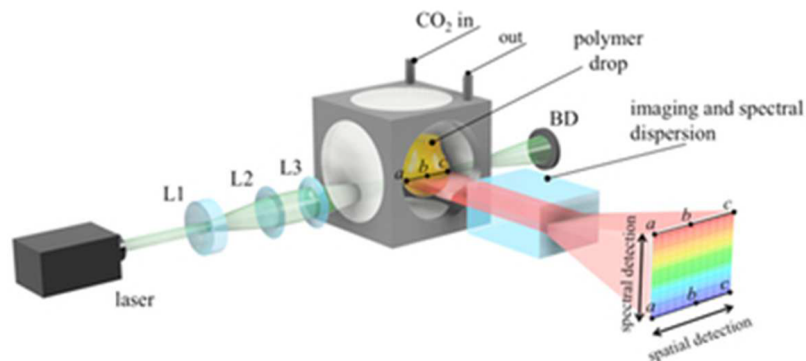


**Figure 1.** Schematic diagram representing the experimental setup for Raman line-imaging.

requires specific information on the polymer/gas solution such as mass transport,<sup>10–12</sup> rheological properties,<sup>13</sup> and thermodynamics.<sup>14</sup> Moreover, the central role played by the specific interactions between the CO<sub>2</sub> molecules and the macromolecular chains has been recognized and requires in-depth study.<sup>15</sup> A number of investigations have recently appeared on mass transport and solubility of CO<sub>2</sub> in PCL<sup>16–18</sup> and the available data have been interpreted mostly by thermodynamic approaches describing the temperature effects on CO<sub>2</sub> solubility. More advanced models based on lattice fluid theory have been also proposed.<sup>16,17</sup> Vibrational spectroscopy techniques, such as Fourier transform infrared spectroscopy (FTIR), attenuated total reflection FTIR (FTIR-ATR), and Raman spectroscopy are powerful tools to deepen the molecular-level understanding of these systems. Attractive features of the above techniques are sensitivity, specificity, and versatility, which affords the straightforward implementation of elaborated experimental set-ups for the *in situ* monitoring of diffusion processes in carefully controlled conditions of temperature and pressure.<sup>19,20</sup> Several experimental approaches have been proposed to investigate CO<sub>2</sub> diffusion under high pressure and in the supercritical regime: an innovative setup based on high-pressure Raman-line imaging is proposed in the present contribution.

Previous works based on FTIR-ATR and FTIR have detected specific interactions between CO<sub>2</sub> and several polymers containing electron-rich units.<sup>19,21</sup> In particular, carbonyl containing polymers [poly(methyl methacrylate, PMMA, polycarbonate, PC, poly(L-lactic acid), PLLA, poly(D-lactic acid), PDLA, PCL] showed, in the presence of dissolved CO<sub>2</sub>, significant shifts of the  $\nu(\text{C}=\text{O})$  vibration.<sup>20,21</sup> Also the spectrum of dissolved CO<sub>2</sub> showed distinct modifications with respect to the unperturbed gas phase: a splitting of the characteristic bending mode was observed, attributed by several authors to the breaking of the CO<sub>2</sub> original symmetry.<sup>21,22</sup>

In the present study an experimental approach is described to monitor *in situ* the CO<sub>2</sub> sorption at elevated pressures (0.62 to 7.1 MPa) in molten PCL. The method is based on a modified Raman line-imaging setup, which allows—after proper calibration—the quantitative measurement of gas concentration in both the *time-resolved* and the *space-resolved* modes.<sup>23</sup> The spectroscopic data gathered in this way were analyzed in terms of perturbation of the spectral features with respect to reference systems to highlight and interpret the effects of the PCL/CO<sub>2</sub> interactions on the vibrational pattern. To this end, quantum chemistry calculations based on the Moeller–Plesset perturbation theory (MP2)<sup>24–26</sup> on model systems simulating the supramolecular aggregates were performed, followed by a

complete normal coordinate analysis for the calculation of the Raman spectra in terms of both frequency and intensity. The above analysis allowed us to identify the main interaction sites on the polymer backbone and to confirm the interaction mechanism. The calculated Raman spectra were found to be in excellent agreement with the experiment, confirming the predictive capabilities of the chosen model chemistry and supporting the proposed molecular structure of the PCL/CO<sub>2</sub> aggregates. These spectra also allowed a deeper interpretation of the observed effects. In particular, it was shown that the specific signatures for the formation of the supramolecular aggregates are to be sought in the vibrational pattern of the CO<sub>2</sub> probe, while neither the carbonyl stretching nor the C–O–C stretching modes of PCL can be reliably used for this purpose.

The PCL–CO<sub>2</sub> system was also analyzed in the framework of an equation of state (EoS) thermodynamic model based upon a compressible lattice fluid theory endowed with specific interactions. The interactional part of the thermodynamic model was tailored to account for the main interaction sites on the polymer backbone and for the detected interaction mechanism that emerged from the experimental and computational study. The predictions of the thermodynamic model in terms of molar volume of the PCL–CO<sub>2</sub> solution and of CO<sub>2</sub> partial molar volume are consistent, respectively, with experimental volumetric measurements and with the Raman results.

## EXPERIMENTAL SECTION

**Materials.** PCL (CAPA 6800) was supplied by Solvay Warrington (Cheshire, WA4 6HB, UK), as a 100% resin in the form of 3 mm pellets, with a weight-average molecular weight,  $\bar{M}_w$  of  $1.0 \times 10^5$  D and a number-average molecular weight,  $\bar{M}_n$  of  $5.2 \times 10^4$  D, with a polydispersity of 1.9. The pellets had a density of 1.158 g/cm<sup>3</sup>, a melting temperature,  $T_m$  = 333 K and crystallinity degree of 58% (DSC). A hemispherical polymer drop was created on the base of a titanium rod with a diameter of 3.15 mm. Details on drop preparation are given elsewhere.<sup>17</sup> CO<sub>2</sub> with a purity of 99.5% was purchased from Linde, Germany.

**Apparatus.** The investigation of gas transport within the molten polymer has been performed by using the apparatus depicted in Figure 1, made up of an optically accessible pressure chamber combined with a Raman line imaging setup.

The optically accessible pressure chamber consisted of a stainless steel vessel equipped with three glass windows. Two windows were arranged line in sight in order to permit the laser

beam to cross the vessel, and the third one was perpendicular to the others allowing the detection of the 90°-scattered light. The chamber was heated by four electric heating cartridges mounted in the corners of the cubic vessel and the temperature control was guaranteed by a controller combined with a Pt100 temperature sensor. Pressurized CO<sub>2</sub> was fed to the chamber by a syringe pump and a pressure sensor indicated the pressure in the vessel. Placed in the center of the optically accessible pressure chamber, a pendant drop of molten polymer hanging from a rod was subjected to the spectroscopic investigation.

The Raman line imaging set up consisted of an excitation part and of a detection part. The excitation part of the Raman line imaging setup consisted of the laser (an energy-doubled continuous wave Nd:YVO<sub>4</sub> with an emission wavelength of  $\lambda = 532$  nm and an output power of 3.5 W), a plan concave lens and two plan convex lenses. The combination of the plan concave lens (L1, o.d. = 1",  $f = -10$  mm) and a plan convex lens (L2, o.d. = 2",  $f = 1000$  mm) was used to expand the diameter of the circular shaped beam to approximately 45 mm. The expanded laser beam was then focused onto the drop by a plan convex lens (L3, o.d. = 2",  $f = 100$  mm). Here, along the waist of the laser beam focus, the laser power was concentrated in an approximately cylindrical volume (whose diameter was assumed to be 100  $\mu\text{m}$  ca.) resulting in a high excitation power and a high spatial resolution.

The detection of the Raman signals from several positions along the waist of the laser beam focus was performed through the detection part of the Raman line imaging setup, as depicted in Figure 1. It consisted of two achromatic lenses, a long-pass filter, and an imaging spectrometer. The Raman signal coming from the drop was detected through a large solid angle by an achromatic lens with a small  $f$ -number (A1, o.d. = 2",  $f = 100$  mm) and the elastically scattered light was blocked by a long-pass filter (LPF, o.d. = 2", LP 532) that transmitted only the red-shifted Raman-Stokes signal. A second achromatic lens (A2, o.d. = 2",  $f = 200$  mm) imaged the waist of the laser beam focus onto the 50  $\mu\text{m}$ -wide entrance slit of the imaging spectrometer (Andor Shamrock 303i, 303 mm focal length, grating with 1200 lines/mm). The signal was detected with an electron multiplying charge-coupled device camera (Andor Newton, 1600  $\times$  400 pixels of 16  $\times$  16  $\mu\text{m}^2$  pixel size) mounted onto the spectrograph. The spectral imaging was realized through the 400-pixel axis of the CCD providing spatial resolution along the dimension of the entrance slit, combined with the 1600-pixel axis providing the spectral resolution. For the experiment, 10 pixels were binned along the spatial axis of the CCD detector, resolving the length of the measurement volume in 40 increments of 64  $\mu\text{m}$  length each. The inelastically scattered light from each of these 40 measurement positions was dispersed in its wavelength components along the 1600-pixel spectral axis of the CCD detector. A ruled reflection grating of 1200 lines per mm optimized for 500 nm resolved a wavelength range of 546 nm up to 605 nm, corresponding to a Raman shift range of 480  $\text{cm}^{-1}$  up to 2270  $\text{cm}^{-1}$ . Accordingly, the Raman signal coming from different measurement positions could be stored on neighboring pixels columns along the spatial axis of the CCD detector. Summarizing, each image acquired with the camera behind the imaging spectrometer is composed of 40 Raman spectra, each one acquired from the 40 64  $\mu\text{m}$ -long increments along the waist of the laser beam focus.

**Testing Procedure.** Tests were performed at 353 K and at CO<sub>2</sub> pressures up to 7.1 MPa. The measuring chamber was first evacuated in order to remove moisture from the polymer

before starting the test; then, a series of 50 back-to-back images was acquired from neat PCL. Each series consisted of 40 Raman spectra, acquired with an exposure time of 6 s from the 40 increments along the waist of the laser beam. Pressurization was then started and, immediately after opening the valve connecting the syringe pump to the chamber, Raman images were recorded every 30 s, until the spectra did not show any variation in time, defining the attainment of equilibrium. Pressure was increased in a stepwise manner. Furthermore, in order to gain information on sorption at equilibrium, a series of 50 equilibrium images of the drop under CO<sub>2</sub> atmosphere were recorded likewise, at each equilibrium pressure. All images were acquired with the same camera settings and with an exposure time of 6 s.

**Computational Methods for Conformational Searching and Quantum Chemistry-Based Normal Coordinate Analysis (QCB-NCA).** Molecular Mechanics (MM) calculations were performed using the MM+ force field, which is an extension of the popular Allinger's MM2 force field.<sup>27,28</sup> The potential energy surface of the model compound was explored by a conformational search algorithm adopting the Monte Carlo multiple minimum (MCM) scheme<sup>29</sup> for systematic variations of the selected dihedrals. All MM computations were made with the programs' suite Hyperchem Pro6, from Hypercube Inc. (Gainesville, FL).

Quantum chemistry calculations were performed using the MP2/6-31G(d) level of theory and basis set.<sup>24–26</sup> Optimizations were started from the minima identified by the MM conformational search in the case of the pentyl hexanoate (PHEX) model compound and from several different initial configurations in the case of the PHEX/CO<sub>2</sub> supramolecular aggregates. The choice of the starting configurations will be discussed in the relative paragraph.

The interaction energies of the complexes, hereafter binding energies,  $E_b$ , for different interaction geometries were calculated in the frame of the *supermolecule* method,<sup>30</sup> as the difference in energy between each complex and the sum of the isolated monomers, each relaxed to their minimum energy configuration

$$\Delta E = E_{AB} - (E_A + E_B) \quad (1)$$

where  $E_{AB}$  is the energy of the optimized complex and  $E_A$  and  $E_B$  are the respective energies of the optimized monomers. By adopting this definition, negative energies favor the aggregate formation. All binding energies were corrected for the basis set superposition errors (BSSE) which is generally non-negligible for the case of weakly bound complexes. BSSE were calculated using the counter-poise method of Boys and Bernardi.<sup>31</sup>

After geometry optimization, a normal coordinate analysis at the same level of theory was performed, comprising the calculation of the Hessian matrix ( $F$ ) by analytical evaluation of the first and second derivatives of the potential energy with respect to the Cartesian displacement coordinates. The  $F$  matrix was then transformed in terms of mass-weighted coordinates and diagonalized to obtain the corresponding eigenvalues (normal frequencies) and eigenvectors (displacement vectors,  $L$  matrix). Finally, a transformation into a set of nonredundant internal coordinates of both the  $F$  and  $L$  matrices was carried out in order to characterize the normal modes in terms of their potential energy distribution (PED), expressed, in normalized form, as<sup>32</sup>

$$(PED)_{jk} = \frac{F_{jj}L_{jk}^2}{\sum_i F_{ii}L_{ik}^2} \times 100 \quad (2)$$

where the PED (in %) is relative to the contribution of the  $j$ th internal coordinate to the  $k$ th normal mode,  $F_{jj}$  is the  $j$ th diagonal force constant and  $L_{jk}$  is the corresponding element of the L matrix. Only the diagonal terms of the F matrix were considered. To take into account anharmonicity effects and the systematic errors associated with the calculated frequencies, these were corrected according to the constant scaling factor approach.<sup>33,34</sup> The QM calculations were performed by the Gaussian 03 program package<sup>35</sup> (Gaussian Inc., Pittsburgh, PA) run on a HP Integrity RX2620 system with two parallel Itanium processors. The results were visualized with the GausView graphic interface (Gaussian Inc.). PED calculations were carried out with the aid of the VEDA program.<sup>36,37</sup>

## RESULTS AND DISCUSSION

**Analysis of PCL/CO<sub>2</sub> Spectra.** In Figure 2 are compared the spectra of neat PCL collected at 353 K (red trace) and of a

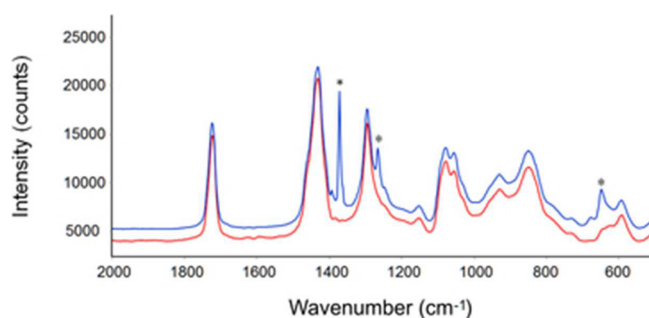


**Figure 2.** Raman spectra of neat PCL (red trace) and PCL/CO<sub>2</sub> solution equilibrated with CO<sub>2</sub> gas at 353 K and 6.2 MPa (blue trace). Asterisks denote CO<sub>2</sub> peaks. The blue trace has been arbitrarily shifted along the Y-axis to facilitate the comparison.

typical PCL/CO<sub>2</sub> solution collected at 353 K and at a CO<sub>2</sub> pressure of 6.2 MPa (blue trace); both spectra were acquired in the center of the drop.

The Raman spectrum of molten PCL is complex, with three fully resolved peaks at 1294, 1430, and 1722 cm<sup>-1</sup>, and a highly overlapped pattern below 1200 cm<sup>-1</sup>. A detailed description of these spectral features in terms of normal modes of vibration will be discussed in the forthcoming paragraph on normal coordinate analysis. The spectrum of the sample equilibrated in gaseous CO<sub>2</sub> clearly shows the characteristic signals of the sorbed molecule at 1371 and 1264 cm<sup>-1</sup>. Toward a deeper analysis of the spectrum of CO<sub>2</sub> dissolved in PCL, we isolated it by use of difference spectroscopy. Thus, the spectrum of neat PCL in the melt state was subtracted from the spectrum of the equilibrated sample until the reference peak at 1431 cm<sup>-1</sup> was reduced to the baseline. The result of this analysis, relative to the sample equilibrated at 6.2 MPa is compared to the spectrum of CO<sub>2</sub> gas (at the same  $T$  and  $P$  values) in Figure 3. Analogous features are observed for the samples equilibrated at the remaining pressures (data not reported). It is immediately apparent that the doublet at 1371–1264 cm<sup>-1</sup> is not the sole feature produced by the solute: besides the satellite bands nearby the main peaks, a doublet occurs at 676–648 cm<sup>-1</sup>. The PCL spectrum is almost completely removed, indicating a negligible perturbation of the vibrational behavior of the matrix

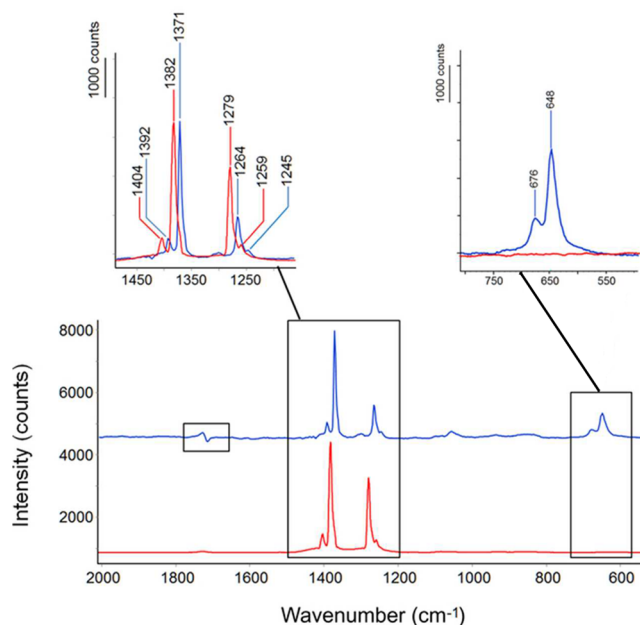


**Figure 3.** Red trace: Raman spectrum of gaseous CO<sub>2</sub> collected at 353 K 6.2 MPa outside the drop. Blue trace: Difference spectrum at 353 K and 6.2 MPa obtained by subtracting the red trace of Figure 2 (neat PCL) from the blue trace of Figure 2 (PCL/CO<sub>2</sub> solution). The difference spectrum is representative of CO<sub>2</sub> dissolved in PLC. The blue trace has been shifted along the Y-axis to facilitate the comparison. The insets compare the difference spectrum with the gas-phase spectrum in two frequency ranges.

material upon CO<sub>2</sub> sorption. The only detectable effect is a first-derivative profile centered at 1722 cm<sup>-1</sup>, which is indicative of a blue-shift of the PCL  $\nu(\text{C}=\text{O})$  vibration. The maximum shift, occurring at  $P = 7.1$  MPa, amounts to +2 cm<sup>-1</sup>.

Returning to the CO<sub>2</sub> spectrum (see Figure 3), we summarize briefly the Raman assignments. The main doublet at 1371–1264 cm<sup>-1</sup> (1382–1279 cm<sup>-1</sup> in the gas phase) is due to the Fermi resonance between the symmetric stretching mode ( $\nu_1$ ) and the first overtone of the bending mode ( $2\nu_2$ ) (Fermi dyad). It is explicitly noted that, because of the  $D_{\infty h}$  symmetry of the isolated CO<sub>2</sub> molecule, the  $\nu_2$  mode is Raman active. The two satellite bands at 1392–1245 cm<sup>-1</sup> (1404–1259 cm<sup>-1</sup> in the gas phase) are hot-bands, i.e. transitions occurring from already excited states.

Both components of the Fermi dyad are red-shifted in the PCL solutions with respect to the gas phase, by –11 and –15 cm<sup>-1</sup>, respectively. These shifts, however, convey the Fermi resonance effects which perturb the true vibrational frequencies of the original transitions. To compensate for these effects and to derive frequency values to be compared with quantum chemistry calculations, we made use of the Howard–Lok model<sup>38</sup> which predicts the unperturbed vibrational frequencies  $\nu_1$  and  $\nu_2$  to be given by

$$\nu_1 = \frac{\nu_h + \nu_l}{2} - \frac{\Delta}{2} \quad (3)$$

$$\nu_2 = \frac{\nu_h + \nu_l}{4} + \frac{\Delta}{4} \quad (4)$$

where  $\nu_h$  and  $\nu_l$  are, respectively, the observed positions of the high-frequency and the low-frequency components of the Fermi dyad, and  $\Delta$  is the separation of the unperturbed

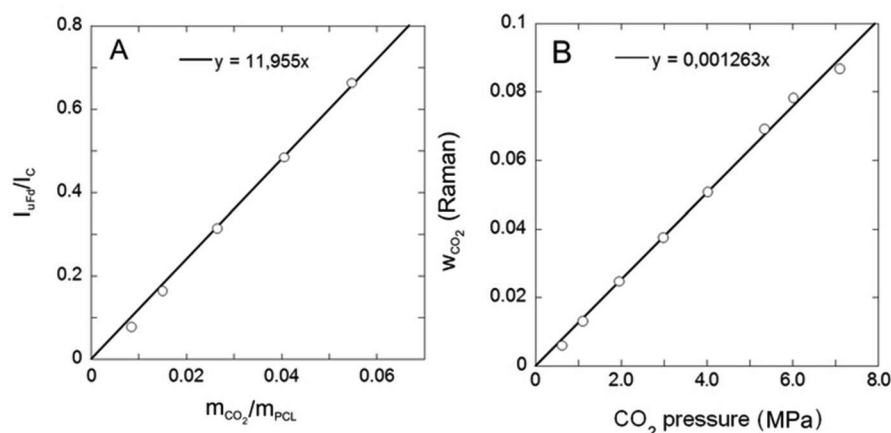


**Figure 4.** (A) Intensity ratio  $\frac{I_{uFd}}{I_c}$  vs mass ratio  $\frac{m_{CO_2}}{m_{PCL}}$ . (B) Mass fraction of penetrant,  $w_{CO_2}$ , as a function of  $CO_2$  pressure.

vibrational levels.  $\Delta$ , in turn, is given by  $\Delta = \sqrt{X^2 - 4W^2}$ , where  $X$  is the observed frequency separation of the two components, and  $W$  is the Fermi coupling constant, estimated to be  $-51.232 \text{ cm}^{-1}$  for  $CO_2$ .<sup>39,40</sup> According to eqs 3 and 4,  $\nu_1$  and  $\nu_2$  for  $CO_2$  dissolved in PCL amount, respectively, to 1302.5 and  $666.2 \text{ cm}^{-1}$ , to be compared with 1326.5 and  $667.8 \text{ cm}^{-1}$  in the gas phase in the same conditions of  $T$  and  $P$ . For comparison,  $\Delta\nu_1 = \nu_{1,CO_2 \text{ sorbed}} - \nu_{1,CO_2 \text{ neat}}$  for  $CO_2$  dissolved in water, where it forms weak molecular interactions of the van der Waals type, is  $-13.5 \text{ cm}^{-1}$ , while  $\Delta\nu_2 = \nu_{2,CO_2 \text{ sorbed}} - \nu_{2,CO_2 \text{ neat}}$  is  $-3.6 \text{ cm}^{-1}$ .<sup>41</sup>

From the observed frequency shifts, it is possible to estimate the average size of the pores in which the  $CO_2$  molecule is accommodated. In the solid state these pores are generally regarded as the free-volume elements present in the system at the test conditions. The estimation results from the cavity model for gas hydrates of Nakahara and co-workers,<sup>42</sup> which considers an uniaxial molecule trapped in a spherical cavity of diameter  $2a$  surrounded by a dielectric medium with permittivity  $\epsilon$ . The carbon atom of the  $CO_2$  molecule is assumed to be located, on average, in the cavity center. Under these assumptions, the model predicts that the vibration frequency in the cavity,  $\nu'$ , can be related to that in vacuum,  $\nu_0$ , through the relationship:

$$\frac{\nu'}{\nu_0} = \left(\frac{1}{\epsilon^*}\right)^2 \quad (5)$$

where  $\epsilon^*$ , the effective permittivity within the cavity, depends on the distance from the cavity center,  $b$  ( $b < a$ ), according to<sup>41,42</sup>

$$\frac{1}{\epsilon^*} = 1 - \frac{\epsilon(\nu) - 1}{\epsilon(\nu) + 0.5} \times \left(\frac{b}{a}\right)^3 \quad (6)$$

from which:<sup>41</sup>

$$\epsilon^* = \frac{1}{c} \int_0^c \frac{db}{1 - \left(\frac{\epsilon-1}{\epsilon+0.5}\right)\left(\frac{b}{a}\right)^3} \quad (7)$$

In eq 5, the vibrational energy of the  $\nu_1$  mode in vacuum is taken at  $1332 \text{ cm}^{-1}$  according to.<sup>41,43</sup> In eq 7,  $c$  is the interatomic distance between carbon and oxygen in  $CO_2$ .  $\epsilon$  is equal to the square of the refractive index of the medium,  $n$ ,

which, in general, depends on  $\nu$ ; for PCL  $n$  is 1.48 and in several polyesters has been demonstrated to remain constant in the whole frequency range of the Raman measurement.<sup>44</sup> Numerical integration of eq 7, combined with eq 5, provides a value of  $2.51 \text{ \AA}$  for the average cavity radius, which corresponds to the average distance between the probe center and the surrounding macromolecular environment. Thus, the pore diameter results to be essentially coincident with the van der Waals diameter of the probe molecule as obtained from the relative equation of state ( $5.2 \text{ \AA}$ ), and from the value reported by Sloan<sup>45</sup> ( $5.1 \text{ \AA}$ ). This result implies that the probe is closely surrounded by PCL macromolecules up to the excluded molecular volume. The situation is close to that realized in  $H_2O$  solution, where the calculated average cavity size is again  $5.0 \text{ \AA}$ .<sup>41</sup> It is informative to compare the above estimation with those from other techniques that allow an evaluation of free-volume in polymer systems. The main method is positron annihilation lifetime spectroscopy (PALS) which, at room temperature and at atmospheric pressure, provided, for the average hole radius, a value of  $2.9 \text{ \AA}$  for both polycarbonate and PMMA,<sup>46</sup>  $2.6 \text{ \AA}$  for poly(ethylene terephthalate),<sup>47</sup>  $3.2\text{--}3.4 \text{ \AA}$  for an alkyd resin,<sup>48</sup> and  $2.5\text{--}2.9 \text{ \AA}$  for a series of bifunctional epoxy resins.<sup>49</sup> On the other hand, Ikeda-Fukazawa and co-workers, in a study based on high-pressure Raman measurements, reported an estimated value of  $1.9 \text{ nm}$  for the diameter of the cavities occupied by  $CO_2$  molecules absorbed in PMMA at room temperature and at  $4.5 \text{ MPa}$  pressure.<sup>50</sup> We conclude that any excess free-volume eventually frozen in the amorphous phase of the polyester at room temperature is suppressed in the pressurized melt and the incoming  $CO_2$  behaves as in a low-molecular liquid solution, where it occupies a volume just corresponding to its size. The estimated cavity radius affords the evaluation of the partial molar volume of  $CO_2$  in the PCL solution, which amounts to  $39.8 \text{ cm}^3/\text{mol}$ , a value not affected by pressure in the investigated range as the frequencies of the Fermi dyad are found to remain constant when pressure increases. In a following section this value will be compared to those arising from calculations based on equation of state modeling of the PCL- $CO_2$  mixture.

It is well-known that the intensities of the Raman signals are directly proportional to the concentration of scattering species.<sup>23,51</sup> In particular, for the present system such a relationship can be expressed as

$$\frac{I_{uFd}}{I_c} = \frac{n_{\text{CO}_2}}{n_{\text{C=O}}} \times K_{cs} = \frac{m_{\text{CO}_2}}{m_{\text{PCL}}} \times \frac{M_{ru}}{M_{\text{CO}_2}} K_{cs} \quad (8)$$

where  $I_{uFd}$  and  $I_c$  are, respectively, the signal intensities of the upper Fermi-dyad and the carbonyl peak,  $n_{\text{CO}_2}$  and  $n_{\text{C=O}}$  are the moles of  $\text{CO}_2$  and carbonyl groups and  $K_{cs}$  is a constant related to the ratio between the Raman cross sections of the two analytical signals. Neglecting end-group effects (a reasonable assumption, given the PCL molecular mass) the moles of  $\text{C=O}$  groups can be assumed equal to the moles of PCL repeating-units, from which follows the right-most expression of eq 8, where  $m_{\text{PCL}}$  and  $m_{\text{CO}_2}$  are the masses of the polymer matrix and of  $\text{CO}_2$ , respectively, and  $M_{ru}$  and  $M_{\text{CO}_2}$  represent the molar masses of the PCL repeating unit and of  $\text{CO}_2$ .

In terms of mass fraction of penetrant,  $w_{\text{CO}_2}$ , we may write

$$w_{\text{CO}_2} = \frac{m_{\text{CO}_2}}{m_{\text{CO}_2} + m_{\text{PCL}}} = \frac{1}{1 + \frac{I_{uFd}}{I_{\text{CO}_2}} \times \frac{M_{ru}}{M_{\text{CO}_2}} \times K_{cs}} \quad (9)$$

The intensity of the upper Fermi dyad, normalized to the intensity of the carbonyl peak of PCL is found to increase linearly as a function of  $\text{CO}_2$  pressure, in the range 0–7.1 MPa. By relating the above intensity ratio with the mass ratio as evaluated gravimetrically,<sup>17,52</sup> a linear correlation is found according to eq 8, which allows us to translate, in the explored pressure range, the spectroscopic signal into absolute concentration values. The isotherm evaluated from the Raman data by use of the slope of the straight line in Figure 4A, is reported in Figure 4B in terms of mass fraction of sorbed  $\text{CO}_2$ .

By collecting the spectra at a fixed position as a function of time, it is possible to monitor the sorption kinetics; the data relative to the experiment at 3.0 MPa, collected at the drop center (see Figure 5) are reported in Figure 6. The pronounced

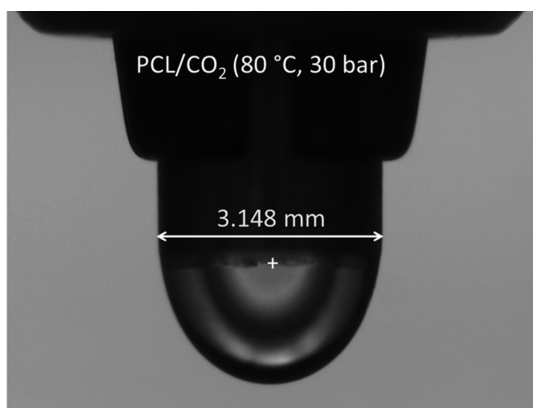


**Figure 5.** Image of the PCL drop attached to the metallic rod. The white cross represents the point where the Raman signal has been acquired to monitor the kinetics of  $\text{CO}_2$  sorption.

induction period is related to the time necessary for the penetrant to reach the sampling area; The diagram displays a coincident shape irrespective of the point where the spectral collection is performed (data not reported), the only difference being related to the length of the induction period which, as expected, decreases when the collection-point gets closer to the drop surface.

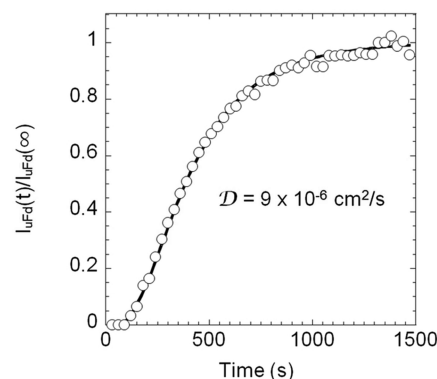


**Figure 6.**  $I_{uFd}(t)/I_{uFd}(\infty)$  vs  $t$  for the measurement carried out at 3.0 MPa. Spectra collected at the drop center. The continuous line represents data fitting performed by assuming Fickian diffusion of  $\text{CO}_2$  in PCL melt eq 10.

To interpret the data reported in Figure 6, it has been assumed that (i) the Fick's law rules the constitutive equation for diffusive mass flux of carbon dioxide, (ii) the polymer swelling during sorption is negligible, and (iii) the intensity of the signal is directly proportional to the  $\text{CO}_2$  concentration (see Figure 4). On the basis of these assumptions, one can predict the time evolution of the signal intensity at the center of the drop (see the position highlighted by the white cross in Figure 5) attached to the metallic rod by considering that carbon dioxide diffusion process within the drop can be schematized as a diffusion process in an hemisphere, with uniform concentration of  $\text{CO}_2$  at the surface and with an impermeable circular base. In turn, invoking symmetry arguments, such a process corresponds to the restriction at the hemisphere domain of the diffusion within a sphere—with a radius equal to the one of the hemisphere—with a constant concentration at the surface. On these grounds, eq 10—reported by Crank<sup>53</sup> for the time evolution of concentration at the center of a sphere for the case of constant surface concentration—has been used to fit the experimental data for  $I_{uFd}(t)/I_{uFd}(\infty)$  vs time at the center of the drop:

$$\frac{I_{uFd}(t)}{I_{uFd}(\infty)} = \frac{C(t)}{C(\infty)} = 1 + 2 \sum_{n=1}^{\infty} (-1)^n \exp\left(-\frac{Dn^2\pi^2t}{R^2}\right) \quad (10)$$

Here  $D$  is the mutual diffusivity for the polymer-carbon dioxide system,  $R$  is the radius of the polymer drop close to the rod (see Figure 6),  $C(t)$  and  $C(\infty)$  are the concentration of  $\text{CO}_2$  within the polymer, respectively at time  $t$  and at equilibrium at the center of the sphere. Using  $D$  as parameter, eq 10 provides an excellent fitting of the spectroscopic data (see Figure 6). The estimated value of diffusivity is equal to  $9 \times 10^{-6} \text{ cm}^2/\text{s}$ , in good agreement with the diffusivity determined from independent gravimetric measurement of sorption kinetics performed at 353 K at pressure values from 0.1 to 4.0 MPa, which span the range of values from  $6 \times 10^{-6}$  to  $1.5 \times 10^{-5} \text{ cm}^2/\text{s}$ .<sup>17,33</sup> This result evidence how the adopted experimental approach, based on Raman spectroscopy, is quite reliable also in providing information on mass transport properties of the system.

**Evaluation of Volumetric Properties for the PCL– $\text{CO}_2$  Mixture from EoS Theory.** To validate the outcomes of vibrational spectroscopy measurements in terms of partial molar volume of  $\text{CO}_2$  in PCL– $\text{CO}_2$  mixtures at different values

of concentration of carbon dioxide at sorption equilibrium, an independent estimate of partial molar volume has been performed. The evaluation of the partial molar volume involves the calculation of the following derivative

$$\tilde{V}_{\text{CO}_2} = \left. \frac{\partial V^{\text{MIX}}}{\partial n_{\text{CO}_2}} \right|_{T, P, n_{\text{polymer}}} \quad (11)$$

where  $\tilde{V}_{\text{CO}_2}$  is the partial molar volume of carbon dioxide,  $V^{\text{MIX}}$  is the volume of the mixture, and  $n$  stands for the number of moles. This derivative cannot be calculated using the available experimental data, which refer to mixture volumes evaluated at different pressures, at sorption equilibrium. To estimate such derivative one would need to know the dependence of mixture volume upon the concentration of  $\text{CO}_2$ , at specified values of  $T$  and  $P$ .

A viable option is to obtain this information from equation of state theories for polymer–penetrant binary mixtures. In fact, such theories provide expressions for both the chemical potential of penetrant within the mixture and for the density of the mixture itself as a function of temperature, pressure, and concentration of penetrant. These expressions can be used to describe equilibrium sorption isotherms of pure low molecular weight penetrants in polymer–penetrant mixtures, making use of a certain number of fitting parameters. Once these parameters are available, one can use these theoretical models to predict the mixture volume at specified values of temperature, pressure and penetrant concentration, also in conditions different from those where sorption equilibrium is attained.

In the case at hand, we have used a compressible lattice EoS theory which accounts for nonrandomicity of contacts in the mixture and for possible penetrant–penetrant, polymer–polymer and penetrant–polymer specific interactions. This theory, proposed by Panayiotou et al.<sup>54,55</sup> and referred to in the following as non-random hydrogen bonding (NRHB) theory, accounts for the establishment of self- and cross-hydrogen bondings. In the present context, the NRHB approach has been used to deal with polymer–carbon dioxide interactions, neglecting polymer–polymer and penetrant–penetrant specific interactions. In particular, on the basis of quantum chemistry calculation on model PCL/ $\text{CO}_2$  aggregates (to be discussed later), corroborated by the outcomes of Raman spectroscopy analysis, it is found that the main interaction is of Lewis acid – Lewis base (LA–LB) type, involving the electron deficient carbon of  $\text{CO}_2$  as electron acceptor and the electron rich oxygen of the  $>\text{C}=\text{O}$  unit as electron donor. Although another cooperative interaction of the  $\text{C}-\text{H}\cdots\text{O}$  type has been detected, in constructing the model we have considered a single interaction type between the PCL carbonyl and  $\text{CO}_2$ , which embraces the dual nature of the actual interaction mechanism.

The model provides a very good fitting of the gravimetric sorption isotherm,<sup>17,52</sup> of  $\text{CO}_2$  in molten PCL at 353 K (see Figure 7) using two fitting parameters, i.e. the mean field interaction parameter,  $k_{12}$ , and the molar Helmholtz energy of formation of the specific  $\text{CO}_2$ –carbonyl interaction,  $A$ . The determined values for model parameters were 0.182 for  $k_{12}$  and  $-11000$  J/mol for  $A$ . On the basis of these parameters, the NRHB model has been used to predict the molar volume of the PCL– $\text{CO}_2$  mixtures. Predictions of theoretical model are in excellent agreement with the experimental data available<sup>17,52</sup> for mixtures at equilibrium with pure  $\text{CO}_2$  (see Figure 8A, B).

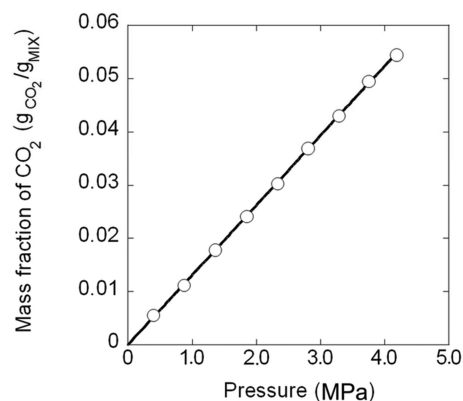


Figure 7. Gravimetric sorption isotherm of  $\text{CO}_2$  in molten PCL at 353 K.<sup>17,52</sup> Continuous line represents data fitting by NRHB theory.

Once the reliability of model predictions has been validated against experimental data, NRHB theory has been used to predict, at each pressure, the partial molar volume of carbon dioxide in the mixture. This value has been obtained by using the following expression:

$$\tilde{V}_{\text{CO}_2} = \hat{V}_{\text{MIX}} + (1 - y_{\text{CO}_2}) \left. \frac{\partial \hat{V}^{\text{MIX}}}{\partial y_{\text{CO}_2}} \right|_{T, P} \quad (12)$$

where  $\hat{V}_{\text{MIX}}$  represents the molar volume of the mixture and  $y_{\text{CO}_2}$  represents the molar fraction of carbon dioxide in the polymer–penetrant mixture. The derivative in eq 12 has been evaluated numerically at each pressure at the corresponding sorption equilibrium concentration of  $\text{CO}_2$ , from the values of molar volume of the mixture provided by the model, at the selected pressure, as a function of values of carbon dioxide concentration in the proximity of equilibrium concentration. The results of this analysis are reported in Figure 9. It is worth noting that the theory provides values for partial molar volume that slightly increase with pressure as opposed to a pressure independent value detected from vibrational spectroscopy. The average value predicted for partial molar volume of  $\text{CO}_2$ , in the range of interest, is  $38,09$   $\text{cm}^3/\text{mol}$ , in good agreement with the value obtained from the vibrational spectroscopy analysis, i.e.,  $39.8$   $\text{cm}^3/\text{mol}$ .

**Ab Initio Calculations and Normal Coordinate Analysis.** We performed a quantum chemistry calculation on model PCL/ $\text{CO}_2$  aggregates; the scope was 2-fold: (i) to identify the most stable supramolecular complex and the preferential site of interaction on the polymer backbone; (ii) to evaluate theoretically the Raman spectra of the adduct according to the normal coordinate method, so as to deepen the interpretation of the spectroscopic results.

Direct application of QCB-NCA methods to model real polymer/ $\text{CO}_2$  systems is impractical because of the large number of atoms involved. When dealing with semicrystalline polymers in the melt or with amorphous polymers a further complication arises from the fact that the molecular geometry is not experimentally available and is to be derived from a careful conformational analysis, which becomes a preliminary and critical step of the NCA. Two distinct approaches are generally employed: in the first the whole macromolecule is considered, or—to be more precise—an oligomer comprising a limited number of monomeric units (4–6, depending on the complexity of the monomer structure). This to restrict the

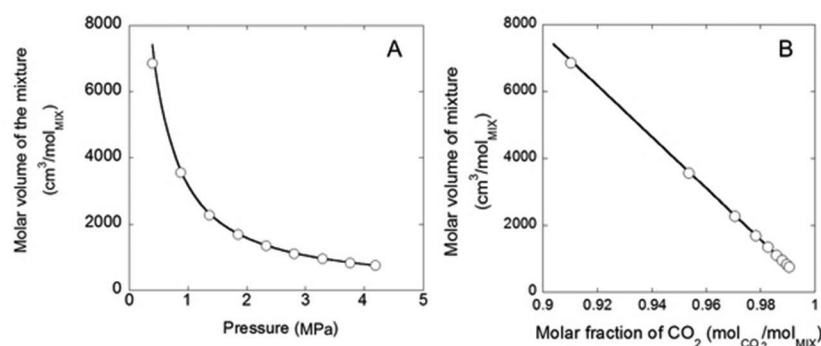


**Figure 8.** (A) Experimentally determined values (white circles) for molar volume of the PCL/CO<sub>2</sub> mixtures reported as a function of pressure at sorption equilibrium<sup>17,52</sup> as compared to predictions by NRHB theory (continuous line). (B) Experimentally determined values (white circles) for molar volume of the PCL/CO<sub>2</sub> mixtures reported as a function of molar fraction of dissolved carbon dioxide, at sorption equilibrium<sup>17,52</sup> as compared to predictions by NRHB theory (continuous line).

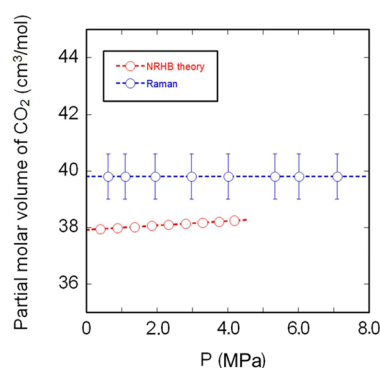


**Figure 9.** Partial molar volume of carbon dioxide in PCL–CO<sub>2</sub> mixtures. Comparison between the values predicted by the NRHB theory (red symbols) and those from Raman spectroscopy (blue symbols). Error bars have been estimated considering the uncertainty in measuring the frequency of the Raman signals.

problem to a manageable size. Reasonable success has been reached along this direction. For instance, Jarmelo et al.<sup>56</sup> reported a conformational analysis followed by normal coordinate calculations of the poly(L-lactic acid), based on molecular mechanics (for conformational searching) and high-level DFT methods (for geometry refinement and force field evaluation). Oligomers up to the pentamer were considered; a reasonable agreement between calculated and observed IR and Raman spectra was achieved. Honda et al.<sup>57</sup> analyzed by the DFT approach an oligomer of poly(p-phenylenevinylene) comprising five phenylene rings and four vinylene moieties, obtaining reliable assignments for all the IR and Raman peaks and the transition dipole moment vectors for each normal mode. Milani et al.<sup>58</sup> reported the vibrational analysis of amorphous fluorinated optical polymers (2,2,4-trifluoro-5-trifluoromethoxy-1,3-dioxole copolymers) based on semi-empirical (for conformational searching) and DFT (for NCA analysis) methods. The drawback of the above strategy is the complex and shallow potential energy surface, which can make it difficult to identify the global minimum and other significant stationary points. The longer the oligomer chain, the more intricate the potential energy surface is.

An alternative approach relies on the use of appropriate low-molecular-weight model compounds suitably chosen to mimic the chain segment where the relevant conformational degree(s) of freedom is (are) localized. A direct comparison among the spectra of the model and the target system serves to confirm

the reliability of the choice. The model may or may not be coincident with the monomeric unit, depending on the molecular environment in the proximity of the freely rotating bond(s). Examples of the successful application of such a method are the contribution of Milani and co-workers,<sup>58</sup> who simulated the vibrational behavior of amorphous fluorinated copolymers by use of representative diads, and the work by Radice et al.<sup>59</sup> who used low molecular weight model compounds to simulate and interpret the IR spectrum of perfluoropolyethers. In the latter contribution IR intensities were also calculated and used to develop a methodology for quantitative analysis.

The low-molecular-weight compound approach has the advantage of an easier conformational analysis, a lower computational cost and the possibility to select symmetric structures, very useful in vibrational analysis. In the light of the above considerations, to simulate the polymer chain we selected a model compound that comprises the potentially active sites, i.e. the electron rich moieties C=O (sp<sup>2</sup> oxygen) and C–O–C (sp<sup>3</sup> oxygen), plus the nearby aliphatic segments to mimic the chemical environment and the steric hindrance in the proximity of the interacting sites. The chosen molecule was Pentylhexanoate (PHEX), whose optimized structure is represented in Figure 10.

Complexes of ether-oxygen/CO<sub>2</sub> and carbonyl-oxygen/CO<sub>2</sub> are bound by weak interactions, mainly originating from dispersion forces. Capturing the properties of such weakly bound aggregates requires high-level theories and large basis sets. The popular methods based on density functional theory

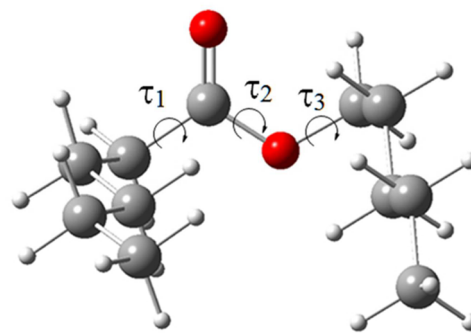


**Figure 10.** Optimized geometry of pentylhexanoate (PHEX). Color code: white = H; gray = C; red = O. For atom numbering refer to Figure S2, Supporting Information.

(DFT) are computationally efficient but not sufficiently accurate to describe the dispersion complexes under investigation.<sup>60–62</sup> We therefore selected the MP2 level of theory and the 6-31(d) standard basis set to perform geometry optimization in the light of previous studies which demonstrated this combination to represent a suitable compromise between accuracy and computational cost.<sup>63,64</sup> Literature results on long-chain, saturated esters of fatty acids<sup>65,66</sup> demonstrated that for this class of compounds the lower energy conformer invariably presents the aliphatic chain in the *all-trans* conformation, and a very satisfactory simulation of the vibrational (Raman) spectrum can be obtained by considering the *all-trans* conformer alone. In view of these results, the conformational search on PHEX was carried out fixing the two aliphatic chains in the *all-trans* conformation and scanning the three conformational degrees of freedom denoted as  $\tau_1$ ,  $\tau_2$ , and  $\tau_3$  in Figure 10.

As expected, the potential energy surface of the PHEX model compound is relatively shallow, with the first four identified minima lying within 1.2 kcal/mol. The most stable conformer identified through the conformational-search algorithm was further refined with the selected model chemistry and subjected to frequency analysis. Among the 99 calculated frequencies no imaginary values were found, thus confirming the nature of the identified stationary point as a true energy minimum. The calculated spectrum is expected to provide information for a deeper interpretation of the complex Raman spectrum of PCL, which is described qualitatively and to a scarce level of detail in the literature.<sup>67</sup>

In Figure 11 is reported a comparison between the observed Raman spectrum of PCL and the calculated Raman spectrum of the PHEX model-compound in the frequency range 530–2000  $\text{cm}^{-1}$ .

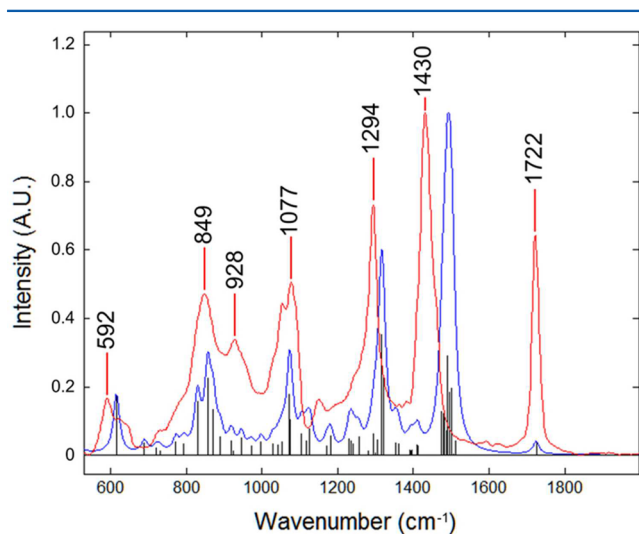


**Figure 11.** Experimental Raman spectrum of PCL (red trace) and calculated Raman spectra of PHEX (blue trace) in the 500–2000  $\text{cm}^{-1}$  range.

According to the QCB-NCA analysis, in the above interval there appear 60 vibrations, most of which with significant intensity (see the bar graph in Figure 11); the observed spectrum is simpler, showing seven major features (1722, 1430, 1294, 1077, 928, 849, 592  $\text{cm}^{-1}$ ) and two unresolved components at 1054 and 625  $\text{cm}^{-1}$ . The simpler appearance of the observed spectrum is due to the normal modes of similar

nature displaying vibrational frequencies very close to each other, thus forming clusters of peaks around specific regions of the spectrum. Introducing an arbitrary spreading function for the Raman scattering to take into account the vibrational relaxation effects (we used a Lorentz function with full width at half-height (fwhh) of 15  $\text{cm}^{-1}$ ) and summing up the resulting intensities over the whole frequency range, we end-up with the simulated spectrum represented as the blue trace in Figure 11. Now we recognize five fully resolved components which nicely correlate with the observed features, both in terms of position and with respect to the normalized intensities. The main peak of the simulated spectrum at 1493  $\text{cm}^{-1}$ , corresponding to the observed at 1430  $\text{cm}^{-1}$ , is made up solely of HCH bending modes (see the potential energy distribution, PED, reported in Table S1, Supporting Information). The second, most intense feature of the calculated spectrum at 1317  $\text{cm}^{-1}$ , corresponding to the peak observed at 1294  $\text{cm}^{-1}$ , comprises three main components due to HCC bending modes with minor contributions from HCCC torsions (13–15%). A further weak component in the low-frequency side originates from the HCO bending, with minor contributions from HCOC and HCCC torsions (see PED, Table S1, Supporting Information). Overall, the feature can be safely assigned to the HCC bending vibrations.

The peak calculated at 1074  $\text{cm}^{-1}$  and observed at 1077  $\text{cm}^{-1}$  comprises only two components, both due to C–C stretching modes and is therefore a typical skeletal vibration. The more complex profile observed experimentally with two distinct relative-maxima is likely due to the well-known conformational sensitivity of these modes coupled with the fact that we have considered one conformer only. The doublet calculated at 858–831  $\text{cm}^{-1}$  and observed at 849  $\text{cm}^{-1}$ , consists of four components whose PED is spread over many internal coordinates with contributions barely reaching 10%. It is impractical to describe the nature of these highly coupled modes, which have limited utility in vibrational analysis. The peak calculated at 616  $\text{cm}^{-1}$  and observed at 592  $\text{cm}^{-1}$  is due to the vibration of the ester group as a whole, with main contributions from the C6–C5 stretching, the O–C=O bending and the >C=O out-of-plane bending. Finally, the C=O stretching mode, calculated at 1727  $\text{cm}^{-1}$  and observed at 1722  $\text{cm}^{-1}$ , is satisfactorily reproduced in terms of frequency but significantly underestimated in terms of intensity. This effect might be due to the neglect of the weak dipole interactions occurring in the polymer bulk, which impact most on the evaluation of the polarizability derivatives. The frequency is not affected though, so that the  $\nu(\text{C}=\text{O})$  mode may represent, in principle, a suitable signature to reveal the occurrence of molecular interactions, due to its essentially isolated nature and the high sensitivity of the peak position to any perturbation of the electron density. On the contrary, the present QCB-NCA analysis demonstrates that the  $\nu(\text{C}-\text{O}-\text{C})$  modes are unsuitable for this purpose because no vibrations can be identified having a total or prevalent  $\nu(\text{C}-\text{O}-\text{C})$  character. The  $\nu(\text{C}-\text{O}-\text{C})$  PED is distributed among highly coupled modes, most of which exhibiting limited intensity. The maximum PED contribution is on the order of 12–13% (see Table S1, internal coordinates s24 and s34), a value insufficient to capture the weak perturbations induced by the molecular interaction with  $\text{CO}_2$ . In principle, the 590  $\text{cm}^{-1}$  peak could be useful because of the presence of the O–C=O bending (25% s57 coordinate); however, it also contains significant contributions from carbonyl modes, which prevents discrim-

ination between the two interaction sites. Moreover, in-plane bendings are far less sensitive than stretchings.

To simulate the PHEX/CO<sub>2</sub> interaction, starting-point structures were manually constructed, to be subsequently optimized with no geometry constraints at the same level of theory as for the two individual components. The choice of the starting-point structures is known to be critical, since the optimization algorithm locates the minimum closer to the initial geometry. In this respect, it has been generally assumed that the carbonyl oxygens (sp<sup>2</sup> O atoms) are the most important sites for CO<sub>2</sub> interactions with ester compounds.<sup>68</sup> Numerous studies identified as a main mechanism a Lewis acid–Lewis base (LA–LB) interaction involving the electron deficient carbon of CO<sub>2</sub> as acceptor and the electron rich oxygen of the >C=O unit as electron donor. From a qualitative point of view, the lone-pairs of the carbonyl oxygen are coplanar with the C=O bond and at 120° from the C=O axis. Thus, a bent-T geometry (Figure S1A,B, Supporting Information) would correspond to the CO<sub>2</sub> carbon pointing directly toward one of the lone-pairs of the electron-donor, which results in a maximized orbital overlapping and a more favorable interaction. In fact, this spatial arrangement was found to be the most stable for a series of >C=O/CO<sub>2</sub> LA–LB adducts investigated in the literature.<sup>64,69–73</sup> In the light of the above considerations, the starting structures were constructed locating the CO<sub>2</sub> probe in the plane of the ester group (the –C–CO–O– group), and setting the C6–O7–C37 angle to 120° (for atom numbering, refer to Figures S3 and S4 in the Supporting Information). The initial O7···C37 distance was set to 3.0 Å in the light of the results of ref 69. Because of the different steric hindrance and atom distances, two bent-T configurations were explored, differing for the orientation of the CO<sub>2</sub> molecule with respect to the C=O axis. These were denoted *alkyl-side* and *ester-side*, respectively and are represented in parts A and B of Figure S1 of the Supporting Information.<sup>74</sup>

More recently, the impact of ether-like ester oxygens (sp<sup>3</sup> O atoms) on CO<sub>2</sub> interaction has been also considered: it was shown that the binding energies of CO<sub>2</sub> with sp<sup>3</sup> oxygens in acetate groups were as large as those associated with isolated ethers and carbonyl sites.<sup>64</sup> This prompted us to explore the latter possible interaction; in this case a T arrangement with the principal molecular axis of CO<sub>2</sub> in the plane of the ester group was chosen as starting geometry in the light of the works of Jamroz et al. and Kilic et al.<sup>63,64,69</sup> According to these authors, this T arrangement corresponds to the CO<sub>2</sub> molecule placed “in-between the lone pairs” of the donor, a situation that might minimize the repulsion between the  $\pi$ -electrons of CO<sub>2</sub> and the lone-pairs of the donor.<sup>69</sup> The initial geometry of the C–O–C/CO<sub>2</sub> complex is reported in Figure S1C of the Supporting Information.

Parts I–II of Figure 12 show the optimized structure of the two sp<sup>2</sup>-O/CO<sub>2</sub> adducts, while Figure 12III represents the sp<sup>3</sup>-O/CO<sub>2</sub> complex.

The most stable complex is structure I, whose binding energy,  $E_b$ , is 1.8 and 1.7 times higher than those of structures II and III, respectively (see Table 3). We discuss first the two >C=O/CO<sub>2</sub> complexes: as a first consideration, the donor–acceptor distance (2.80 Å) is consistent with the average distance between the probe center and the surrounding macromolecular environment that we have experimentally evaluated by use of the cavity model (2.51 Å). Second, the considerable  $E_b$  difference suggests the occurrence of multiple

**Table 1.** Observed Frequencies and the Results of the QCB-NCA Analysis (Calculated Frequencies,  $\Delta\nu$ , and PED) for the  $\nu(\text{C}=\text{O})$  Normal Modes of Isolated PHEX and for the Three Investigated PHEX–CO<sub>2</sub> Complexes<sup>a</sup>

	freq obsd (cm <sup>-1</sup> )	freq calcd (cm <sup>-1</sup> )	err (%)	PED (%)	$\Delta\nu$ obsd (cm <sup>-1</sup> )	$\Delta\nu$ calcd (cm <sup>-1</sup> )
PHEX	1722	1727	0.3	84 R	–	–
[PHEX···CO <sub>2</sub> ] <sub>I</sub>	1724	1710	0.8	83 R	+2	–17
[PHEX···CO <sub>2</sub> ] <sub>II</sub>	1724	1716	0.4	84 R	+2	–11
[PHEX···CO <sub>2</sub> ] <sub>III</sub>	1724	1722	0.1	84 R	+2	–5

<sup>a</sup>R = str (C<sub>6</sub>O<sub>7</sub>). Subscripts to complex codes refer to structure numbering in Figure 12.

effects on structure stability. It has been postulated that, besides the main LA–LB mechanism, another cooperative interaction can occur in carbonyl/CO<sub>2</sub> complexes, due to a specific type of hydrogen-bonding formed in systems with H atoms attached to the carbonyl carbon or to the  $\alpha$ -carbon (as in the present case). This C–H···O occurs because of the slight negative charge on the O atoms of CO<sub>2</sub>, which may act as a (weak) proton acceptor, and the slight positive character of the H atom in the above positions. It is not permitted if the hydrogen is located further away from the carbonyl. These interactions are rather weak compared to conventional X–H···Y H-bonding and were found to produce a shortening of the C–H bond length and a blue-shift of the  $\nu(\text{C–H})$  frequencies, the opposite of what is generally observed for conventional H-bonding.<sup>72,74–76</sup> The role of these C–H···O H-bonds is now widely accepted in determining macromolecular conformation,<sup>74,77,78</sup> crystal packing,<sup>79–81</sup> stabilization of inclusion complexes,<sup>82,83</sup> molecular recognition processes,<sup>84,85</sup> and activity of biomolecules.<sup>86,87</sup>

Inspection of structure I identifies one of these interactions at the O38···H23 position, with a H···O distance of 2.72 Å and a C···O distance of 3.39 Å, well within the limits to qualify the interaction as a C–H···O H-bond (4.0 Å).<sup>88</sup> Another close contact at the position O38···H22 (H···O distance = 2.85 Å; C···O distance = 3.31 Å) cannot provide interaction because the H atom is in  $\beta$  to the carbonyl: it produces an unfavorable steric-hindrance effect. The cooperative character of the LA–LB and the C–H···O interactions makes it difficult to separate the contribution of the two mechanisms. However, an estimate of their relative impact can be attempted on the basis of geometrical considerations. In the case of a purely LA–LB mechanism, the two CO<sub>2</sub> oxygens are expected to be equivalent, thus producing two identical C=O bond lengths ( $r$ ). H-bonding will produce the elongation of the involved C=O bond ( $r_1$ ) with respect to the “free” bond ( $r_2$ ) and this effect provides a strong evidence for the occurrence of the C–H···O interaction. Furthermore, the difference between the two bond lengths,  $\Delta r$  is correlated with the H-bonding strength:  $\Delta r$  increases as the interaction gets stronger.<sup>72</sup> For structure I,  $r_1$  is 1.181 Å,  $r_2$  is 1.178 Å and  $\Delta r$  is 3.3 mÅ. These values confirm the establishment of a single C–H···O interaction acting cooperatively with the main LA–LB mechanism, which is slightly stronger than those found for a methyl acetate/CO<sub>2</sub> complex of similar geometry ( $\Delta r = 2.73$ – $2.50$  mÅ).<sup>72</sup>

For structure II, one of these interaction sites is identified at the position O36 – H25; its H···O distance is 2.74 Å and the C···O distance is 3.584 Å. Here again, a second close contact is found at the O38 – H27 position (H···O distance = 2.835 Å, C···O distance = 3.815 Å), which produces a steric-hindrance effects because of the  $\beta$  position of the H atom. In this case, the

**Table 2.** Observed Frequencies and the Results of the QCB-NCA Analysis (Calculated Frequencies,  $\Delta\nu$  and PED) for the CO<sub>2</sub> Vibrations in the Three Investigated PHEX–CO<sub>2</sub> Complexes<sup>a</sup>

	freq obsd (cm <sup>-1</sup> )	freq calcd (cm <sup>-1</sup> )	err (%)	PED (%)	approx descr	$\Delta\nu$ obsd (cm <sup>-1</sup> )	$\Delta\nu$ calcd (cm <sup>-1</sup> )
CO <sub>2</sub>	1327	1284	3.4	50 T <sub>1</sub> , 50 T <sub>2</sub>	$\nu_s(\text{CO}_2)$	–	–
	668	612	8.4	100 $\delta$	$\delta(\text{CO}_2)$	–	–
[PHEX...CO <sub>2</sub> ] <sub>I</sub>	1303	1272	2.4	49 T <sub>1</sub> , T <sub>2</sub>	$\nu_s(\text{CO}_2)$	–24	–12
	676	621	8.1	97 $\delta$	$\delta_{\text{oop}}(\text{CO}_2)$	–6	–0.5
	648	602	7.1	–99 w	$\delta_{\text{ip}}(\text{CO}_2)$	–	–
[PHEX...CO <sub>2</sub> ] <sub>II</sub>	1303	1272	2.4	50 T <sub>1</sub> , 50 T <sub>2</sub>	$\nu_s(\text{CO}_2)$	–24	–12
	676	621	8.1	88 w	$\delta_{\text{oop}}(\text{CO}_2)$	–6	–0.5
	648	604	6.8	98 $\delta$	$\delta_{\text{ip}}(\text{CO}_2)$	–	–
[PHEX...CO <sub>2</sub> ] <sub>III</sub>	1303	1270	2.5	50 T <sub>1</sub> , 50 T <sub>2</sub>	$\nu_s(\text{CO}_2)$	–24	–14
	676	618	8.6	94 $\delta$	$\delta_{\text{oop}}(\text{CO}_2)$	–6	–0.5
	648	605	6.6	77 w	$\delta_{\text{ip}}(\text{CO}_2)$	–	–

<sup>a</sup>T<sub>1</sub> = str(O<sub>36</sub>C<sub>37</sub>); T<sub>2</sub> = str(C<sub>37</sub>O<sub>38</sub>);  $\delta$  = bnd(O<sub>36</sub>C<sub>37</sub>O<sub>38</sub>); w = oop bnd(O<sub>38</sub>O<sub>7</sub>O<sub>36</sub>C<sub>37</sub>). For atom numbering see Figures S3 – S5, Supporting Information.

$r_1$  bond length is 1.180 Å while  $r_2$  is 1.179 Å and  $\Delta r$  is 0.9 mÅ: the H-bonding interaction is still present but is weaker, which is reflected in a lower stabilization energy. However, the slightly reduced H-bonding strength cannot account for the almost doubled binding energy of I: the effect is to be ascribed to the steric hindrance of the bulky pentyl substituent. By inspection of the starting geometry of the >C=O/CO<sub>2</sub> complex *ester-side*, the interaction site appears to be crowded; to reduce the steric effect, the CO<sub>2</sub> molecule is forced to occupy a position far from that required for an optimum overlap with the sp<sup>2</sup> orbital of the electron-donor. In fact, in the relaxed structure the CO<sub>2</sub> carbon is significantly out-of-plane with respect to the reference ester-group plane (the O8–C6–O7–C37 dihedral angle is –34.2°) and the C6–O7–C37 angle amounts to 144.7°. This is not the case with the starting structure *alkyl-side*, for which a more favorable situation around the electron-donor is realized. In this case the relaxed geometry is closer to the initial and retains a significant directionality: the CO<sub>2</sub> carbon is nearer to the ester plane (C5–C6–O7–C37 dihedral = –23.1°) and the C6–O7–C37 angle is 126.60°, very close to the 120° natural angle of the trigonal sp<sup>2</sup> orbital involved in the interaction.

The same considerations can be applied to structure III: in terms of atom charges as evaluated by the Mulliken scheme,<sup>89</sup> the unperturbed PHEX molecule displays a value of –0.643 for the sp<sup>3</sup> oxygen and of –0.598 for the sp<sup>2</sup>-oxygen. Initially, therefore, the two electron-donors have comparable affinity toward the acceptor, with the ester oxygen slightly more reactive than the carbonyl. However, in the former case both the alkyl substituents contribute to hinder the sp<sup>3</sup> interaction-site, pushing the CO<sub>2</sub> molecule out of the optimum overlapping position with the donor orbitals. This is reflected in a binding energy halved with respect to that of structure I. Inspection of the first 10 local minima identified by the MM conformational search indicates that, while in a few cases the situation at the carbonyl position is reversed, that is, the steric hindrance on the *alkyl-side* is slightly higher than that on the *ester-side*, the sp<sup>3</sup> oxygen is invariably less favorable than carbonyl because of the cooperative effect of the two alkyl substituents.

In summary, the QC analysis indicates that the stability of the supramolecular complex is controlled more by the accessibility of the donor than by its electron-density. Accessibility is the key-factor which regulates not only the geometry of the complex but also the specific interaction-site involved in binding. The results reported in<sup>64</sup> corroborate this conclusions: when the steric hindrance of the substituents is

lower, as in isopropyl acetate, the  $E_b$  values of complexes resembling those in parts I and II of Figure 12 are very close to each other (from 3.8 to 3.4 kcal/mol).

Returning to structure I, the complex displays all the characteristic signatures of a moderately strong LA–LB interaction. In particular, a significant effect on the probe molecule is the distortion from linearity with an angle (denoted  $\beta$ ) that differs more and more from the initial value of 180° as the binding energy increases. In fact, a linear relationship has been demonstrated between  $\beta$  and  $E_b$  for a wide range of donor complexes with CO<sub>2</sub>, among which H<sub>2</sub>O, alcohols, ethers, aldehydes, ketones, amines and nitriles.<sup>69</sup> This trend is confirmed in the present study (see Table 3) and the binding energy of structure I is in excellent agreement with the value interpolated from the  $E_b$  vs  $\beta$  curve of ref 69 (3.2 vs 3.3 kcal/mol). The distortion of the linear geometry of the probe brings about important consequences: the original  $D_{\infty h}$  symmetry is transformed into a (local)  $C_{2v}$  symmetry, which activates the bending mode previously forbidden and removes the degeneracy of the in-plane and out-of-plane vibrations. Accordingly, while the calculated spectrum of isolated CO<sub>2</sub> correctly predicts zero Raman activity for  $\delta(\text{CO}_2)$ , finite values of Raman activities are obtained for both in-plane and out-of-plane  $\delta(\text{CO}_2)$  for the three investigated PHEX/CO<sub>2</sub> complexes (see Table 2), with the intensity of the in-plane mode exceeding that of the out-of-plane vibration, as experimentally observed. This analysis confirms that the doublet appearing at 676–648 cm<sup>-1</sup> in the spectra of the PCL/CO<sub>2</sub> solutions originates from the CO<sub>2</sub> bending modes; it is remarked that the 676–648 cm<sup>-1</sup> doublet is to be considered as a specific signature for the occurrence of an attractive interaction of the probe with the substrate since, contrary to the other CO<sub>2</sub> spectral features, it appears only if the interaction takes place and a significant distortion from linearity is induced (see the rightmost inset of Figure 3). With respect to the shift induced by the interaction, it is found that the calculated values correctly predict the direction of the frequency change (a *red-shift* for both  $\nu_s(\text{CO}_2)$  and  $\delta_{\text{oop}}-\delta_{\text{ip}}(\text{CO}_2)$  modes, but the magnitude of the effect is considerably underestimated by the theoretical model ( $\Delta\nu$  goes from –12 to –25 cm<sup>-1</sup> for the  $\nu_s(\text{CO}_2)$  mode in passing from the calculated to the observed value and from –0.5 to –6 cm<sup>-1</sup> for the  $\delta(\text{CO}_2)$  modes. This is related to the fact that the model treats the supramolecular aggregate as isolated *in vacuo* and, therefore, does not take into account the cavity effect discussed in detail in the previous paragraph, which

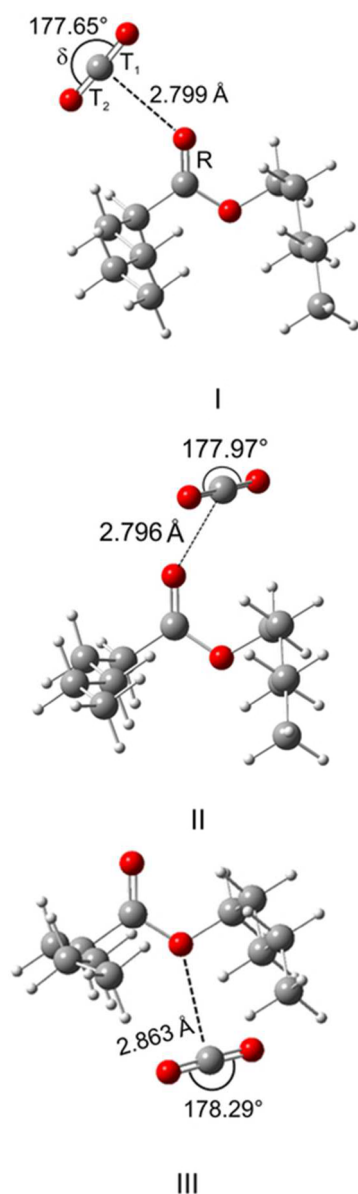


**Figure 12.** Optimized structures of the three investigated PHEX/CO<sub>2</sub> complexes. Color code: white = H; gray = C; red = O. For atom numbering refer, respectively, to Figures S3, S4, and S5, [Supporting Information](#).

was shown to affect markedly the observed frequency of the vibrations.

With respect to the electron donor, the C=O bond of the ester is found to be elongated as compared to the unperturbed structure (from 1.222 to 1.229 Å, 0.6%) and the relative force

constant decreases from 12.717 to 12.521 mdyne/Å, i.e., by 1.54%, which is again a strong evidence of an established LA–LB interaction. For comparison, the interaction of the same carbonyl group with H<sub>2</sub>O, which is of the hydrogen-bonding type and hence considerably stronger, produces a force-constant lowering of 2.15%.<sup>90</sup> The above effects, a direct consequence of the electron-density withdrawing from the Oxygen donor toward the C acceptor, suggest that the  $\nu(\text{C}=\text{O})$  position and, in particular, its downward shift, would positively identify the occurrence of the LA–LB interaction, both for the sensitivity of the Force-constant and because of the essentially isolated nature of the vibration [PED = 84%  $\nu(\text{C}=\text{O})$ ]. According to the theoretical model, the PHEX carbonyl stretching is predicted to be red-shifted by  $-17\text{ cm}^{-1}$  as compared to the unperturbed position (see [Table 1](#)), a result that is to be reconciled with the observed blue-shift of  $+2\text{ cm}^{-1}$ .

To interpret this apparent discrepancy we recall that the observed carbonyl-shift is the ultimate result of several effects. In the first place the band originates from the superposition of two components, the first one being due to interacting carbonyls (at lower frequency, according to the QCB-NCA) and the second originating from the unperturbed (free) carbonyls. Their experimental resolution can be achieved if their separation is significantly larger than their full width at half-height (fwhh). Otherwise, the overlapping of the two components will produce a single band (possibly with a shoulder) and the net effect will consist of a lowering of the peak maximum which gets more pronounced as the intensity of the low-frequency component increases, i.e., as the concentration of interacting carbonyls grows. On these premises, we have developed a simple model to simulate the  $\nu(\text{C}=\text{O})$  band-shape and position. The unperturbed peak is adequately described by a single Gaussian centered at  $1721.5\text{ cm}^{-1}$ , with a fwhh of  $21\text{ cm}^{-1}$  (see [Figure 13](#)), which was, therefore, the adopted band-shape function. The second component was centered  $17\text{ cm}^{-1}$  below ( $1704.5\text{ cm}^{-1}$ ), with the same fwhh and band-shape, assuming a negligible influence of the molecular interaction on the Raman cross-section of the band. This assumption was checked by comparing the theoretically calculated values of Raman activity,  $R_i$ ; which provided comparable values for bound and free carbonyls [ $R(\text{C}=\text{O})_b/R(\text{C}=\text{O})_f = 1.7$ ].

Thus, the model equation can be expressed as

$$I(\nu) = \exp\left[-2.7726\frac{(\nu - \nu_1^0)^2}{\text{fwhh}_1^2}\right] \times X_1 + \exp\left[-2.7726\frac{(\nu - \nu_2^0)^2}{\text{fwhh}_2^2}\right] \times X_2 \quad (13)$$

**Table 3.** Geometrical Parameters, Force Constants and Binding Energies for the Isolated Components and the Three Investigated PHEX–CO<sub>2</sub> Complexes<sup>a</sup>

	$d$ (Å)	$r$ (Å)	$\alpha$ (deg)	$\beta$ (deg)	$F_r$ (mdyn/Å)	$E_b$ (kcal/mol)
CO <sub>2</sub>	–	–	–	180	–	–
PHEX	–	1.222	–	–	12.717	–
[PHEX⋯CO <sub>2</sub> ] <sub>I</sub>	2.799	1.229	126.60	177.65	12.521	3.4
[PHEX⋯CO <sub>2</sub> ] <sub>II</sub>	2.798	1.223	144.76	177.97	12.607	1.9
[PHEX⋯CO <sub>2</sub> ] <sub>III</sub>	2.863	1.221	–	178.29	12.671	2.0

<sup>a</sup>For the meaning of the geometrical parameters ( $d$ ,  $r$ ,  $\alpha$  and  $\beta$ ) refer to Figure S1, [Supporting Information](#).

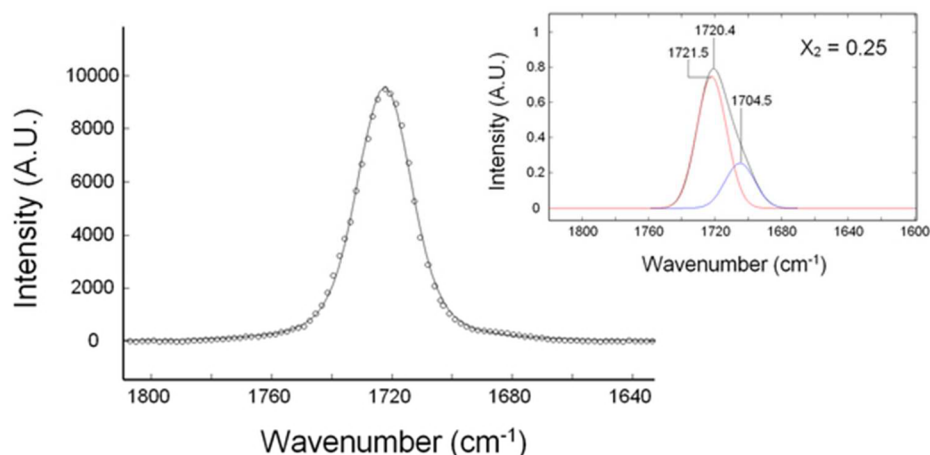


**Figure 13.** Band shape analysis of pure PCL. The inset displays the simulated carbonyl band of a PCL/CO<sub>2</sub> solution with  $X_2 = 0.25$ .

where  $I$  is the normalized intensity of the carbonyl peak (changing from 0 to 1) and  $\nu^0$  is the invariant peak position. The subscripts 1 and 2 refer to the unperturbed and the interacting components, respectively.  $X$  represents the molar fraction of the respective carbonyl populations: assuming that all CO<sub>2</sub> molecules are bound to carbonyls,  $X_2$  is experimentally available from eq 8 as

$$X_2 = \frac{n_b}{n_b + n_f} = \frac{n_{\text{CO}_2}}{n_{\text{C=O}}} = \frac{I_{\text{bfd}}}{I_c} \cdot \frac{1}{K_{\text{cs}}} \quad (14)$$

while  $X_1$  is obtained from the mass-balance as  $X_1 = 1 - X_2$ .

The maximum value of  $X_2$  is 0.25, indicating that noninteracting carbonyls represent the prevailing species in the whole pressure range. According to the simulations, the contribution of the interacting carbonyls produces only a slight broadening of the main peak, which develops a barely discernible asymmetry in the down-side (see inset of Figure 13). No separate components or shoulders are detectable, which is in line with the experimental observations. A gradual *red-shift* is predicted (see Figure 14, curve A); however the overall effect is very low in comparison to the *red-shift* of the interacting component ( $-17 \text{ cm}^{-1}$ ) because of the concentration effect: its maximum value amounts to  $-1.1 \text{ cm}^{-1}$ . The opposite trend of the observed peak-positions (gradual *blue-*

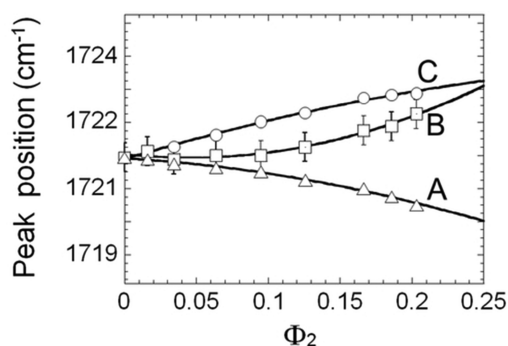


**Figure 14.** (A) Peak position of the carbonyl peak as a function of  $\Phi_2$  as obtained by band-shape simulation. (B) Experimental  $\nu(\text{C=O})$  position vs  $\Phi_2$  and (C)  $\nu(\text{C=O})$  position vs  $\Phi_2$ ; simulation performed summing the dielectric (KBM) effect and the interaction-induced effect.

*shift* with a maximum of  $+2.0 \text{ cm}^{-1}$ , see Figure 14, curve B) indicates the superposition of a second effect.

In general, the medium affects the vibrational frequencies of a molecule through its dielectric constant  $\epsilon$  according to the Kirkwood–Bauer–Magat (KBM) equation, which, in its more general formulation reads<sup>91,92</sup>

$$\frac{\nu_0 - \nu_s}{\nu_0} = \frac{C(\epsilon - 1)}{2\epsilon + 1} \quad (15)$$

In eq 15  $\nu_0$  is the unperturbed frequency (in the present case, the carbonyl frequency in the gas-phase),  $\nu_s$  is the same frequency in solution and  $C$  is a constant depending on the dimensions and dipole properties of the vibrating unit.

The relative shift in the left-side of eq 15 is an increasing function of  $\epsilon$ , which implies that  $\nu_s$  raises, i.e. *blue-shifts* when  $\epsilon$  decreases if dielectric effects are dominant. The lowering of  $\epsilon$  with CO<sub>2</sub> sorption is accounted for considering that the dielectric constant of CO<sub>2</sub> in the liquid is 1.5,<sup>93</sup> a value considerably lower than that of neat PCL (2.19).

Assuming ideal behavior for the PCL/CO<sub>2</sub> solution, the dielectric constant as a function of composition can be estimated from the knowledge of the  $\epsilon$  values of the pure components ( $\epsilon_1$  for PCL and  $\epsilon_2$  for CO<sub>2</sub>) and their relative molar fractions  $\Phi_1$  and  $\Phi_2$ , according to  $\epsilon = \Phi_1\epsilon_1 + \Phi_2\epsilon_2$ . In particular,  $\Phi_2$ , not to be confused with  $X_2$ , is obtained from eq 14 according to

$$\Phi_2 = \frac{n_{\text{CO}_2}}{n_{\text{C=O}} + n_{\text{CO}_2}} = \frac{1}{\frac{1}{X_2} + 1} \quad (16)$$

and  $\Phi_1$  is provided by the mass-balance.

The carbonyl-peak position, as regulated by dielectric effects only, is given by

$$\nu_s'' = \nu_0 - \frac{\nu_0}{K} + \frac{\nu_s'}{K} \quad (17)$$

where  $\nu_s'$  and  $\nu_s''$  are, respectively, the peak-positions in pure PCL and in a PCL/CO<sub>2</sub> solution of a given composition and the constant  $K$  represents the ratio

$$K = \frac{\epsilon' - 1}{2\epsilon' + 1} \times \frac{2\epsilon'' + 1}{\epsilon'' - 1} \quad (18)$$

As in eq 17, primed and double-primed symbols refer, respectively, to the  $\epsilon$  values in neat PCL and in solution ( $\epsilon' =$

$\epsilon_1$ ).  $\nu_0$ , the reference position, is taken as the  $\nu(\text{C}=\text{O})$  frequency of methyl acetate in the gas-phase<sup>94</sup> ( $1761\text{ cm}^{-1}$ ).

The KBM shift (data not reported) increases linearly with composition, reaching a maximum value of  $2.53\text{ cm}^{-1}$  at  $\Phi_2 = 0.20$ . Summing the shifts evaluated by band-shape analysis with those from the KBM equation, we end-up with the overall effect as simulated by considering both the dielectric and the interaction-induced effects. The results are reported in curve C of Figure 14. The comparison with experiment is very satisfactory, with an average discrepancy of  $0.50\text{ cm}^{-1}$ . The analysis confirms that the observed values arise from the contribution of two competing effects, with the dielectric contribution slightly more pronounced and hence prevailing over the interaction-induced effect. The results also indicate that, despite the significant perturbation brought about by the LA–LB interaction, the  $\nu(\text{C}=\text{O})$  mode is not suitable to trace the establishment of the interaction.

## CONCLUDING REMARKS

A molecular-level characterization of the PCL/CO<sub>2</sub> system has been undertaken by high-pressure, line-imaging Raman spectroscopy coupled with *ab initio* quantum chemistry calculations. The following conclusions were drawn:

- The experimental approach described in the present contribution is well suited for the quantitative analysis of CO<sub>2</sub> diffusion in PCL in high pressure regimes, with the added benefit of providing both *time-resolved* and *space-resolved* information.
- The molecular information contained in the vibrational pattern discloses relevant details on free-volume effects and on the interactions among the system components. In particular, it was found that, in the investigated pressure range, the dissolved probe occupies a volume essentially coincident with its van der Waals volume; an estimation of the CO<sub>2</sub> partial molar volume based on the Raman data resulted to be in excellent agreement with values obtained from thermodynamic arguments and showed no dependence on pressure. Lewis acid–Lewis base was confirmed to be the main interaction mechanism, although QC analysis evidenced the occurrence of weak H-bonds acting cooperatively to stabilize the supramolecular complex. The LA–LB contacts were found to be established preferentially with PCL carbonyls. Accessibility of the electron-donor site, i.e., the steric hindrance exerted by the neighboring substituents, regulates both the complex geometry and the specific interaction site.
- From a vibrational point of view, the probe doublet at  $676\text{--}648\text{ cm}^{-1}$  was identified as a specific signature for the occurrence of LA–LB interactions with the substrate. This feature is diagnostic because it only appears when the interactions are formed. On the other hand, despite the significant perturbation brought about by the probe, none of the PCL spectral features can be used to trace the interaction establishment.
- Thermodynamic analysis of the PCL–CO<sub>2</sub> system, in the framework of an equation of state (EoS) thermodynamic model based upon a compressible lattice fluid theory endowed with specific interactions, provided predictions for molar volume of PCL–CO<sub>2</sub> solution and for CO<sub>2</sub> partial molar volume which were consistent, respectively, with experimental volumetric measurements and with the

Raman results. The interactional part of the thermodynamic model was properly tailored to account for the interaction mechanism that emerged from quantum chemistry calculation and experimental Raman spectroscopy analysis.

## ASSOCIATED CONTENT

### Supporting Information

The Supporting Information is available free of charge on the ACS Publications website at DOI: 10.1021/acs.jpcc.6b02438.

Initial configurations of the donor–acceptor complexes, atom numbering for the isolated pentylhexanoate (PHEX) molecule and for the investigated PHEX/CO<sub>2</sub> complexes, and definition of internal coordinates and PED for the isolated PHEX molecule and for the investigated PHEX/CO<sub>2</sub> complexes (PDF)

## AUTHOR INFORMATION

### Corresponding Author

\*(P.M.) E-mail: [pellegrino.musto@ipcb.cnr.it](mailto:pellegrino.musto@ipcb.cnr.it). Telephone: +039 081 8675202.

### Notes

The authors declare no competing financial interest.

## ACKNOWLEDGMENTS

Dr. P. La Manna, from the Institute on Polymers Composites and Biomaterials, National Research Council of Italy, is acknowledged for his contribution to the data analysis.

## REFERENCES

- (1) Bezwada, R. S.; Jamiolkowski, D. D.; Lee, I. Y.; Agarwal, V.; Persival, J.; Trenkenthin, S.; Erneta, M.; Suryadevara, J.; Yang, A.; Liu, S. Monocryl(R) Suture, a New Ultra-Pliable Absorbable Monofilament Suture. *Biomaterials* **1995**, *16* (15), 1141–1148.
- (2) Abedalwafa, M.; Wang, F. J.; Wang, L.; Li, C. J. Biodegradable Poly-Epsilon-Caprolactone (Pcl) for Tissue Engineering Applications: A Review. *Rev. Adv. Mater. Sci.* **2013**, *34* (2), 123–140.
- (3) You, Y.; Min, B.-M.; Lee, S. J.; Lee, T. S.; Park, W. H. In Vitro Degradation Behavior of Electrospun Polyglycolide, Polylactide, and Poly(Lactide-Co-Glycolide). *J. Appl. Polym. Sci.* **2005**, *95*, 193–200.
- (4) Bhattarai, S. R.; Bhattarai, N.; Viswanathamurthi, P.; Yi, H. K.; Hwang, P. H.; Kim, H. Y. Hydrophilic Nanofibrous Structure of Polylactide; Fabrication and Cell Affinity. *J. Biomed. Mater. Res., Part A* **2006**, *78A* (2), 247–257.
- (5) Hao, J.; Yuan, M.; Deng, X. Biodegradable and Biocompatible Nanocomposites of Poly(Caprolactone) with Hydroxyapatite Nanocrystals: Thermal and Mechanical Properties. *J. Appl. Polym. Sci.* **2002**, *86*, 676–683.
- (6) Natarajan, V.; Krithica, N.; Madhan, B.; Sehgal, P. K. Preparation and Properties of Tannic Acid Cross-Linked Collagen Scaffold and Its Application in Wound Healing. *J. Biomed. Mater. Res., Part B* **2013**, *101B* (4), 560–567.
- (7) Woodruff, M. A.; Huttmacher, D. W. The Return of a Forgotten Polymer-Polycaprolactone in the 21st Century. *Prog. Polym. Sci.* **2010**, *35* (10), 1217–1256.
- (8) Dash, T. K.; Konkimalla, V. B. Poly-E-Caprolactone Based Formulations for Drug Delivery and Tissue Engineering: A Review. *J. Controlled Release* **2012**, *158* (1), 15–33.
- (9) Duarte, A. R. C.; Mano, J. F.; Reis, R. L. Supercritical Fluids in Biomedical and Tissue Engineering Applications: A Review. *Int. Mater. Rev.* **2009**, *54* (4), 214–222.
- (10) Goel, S. K.; Beckman, E. J. Generation of Microcellular Polymeric Foams Using Supercritical Carbon-Dioxide 0.1. Effect of Pressure and Temperature on Nucleation. *Polym. Eng. Sci.* **1994**, *34* (14), 1137–1147.

- (11) Han, J. H.; Dae Han, C. Bubble Nucleation in Polymeric Liquids 0.1. Bubble Nucleation in Concentrated Polymer-Solutions. *J. Polym. Sci., Part B: Polym. Phys.* **1990**, *28* (5), 711–741.
- (12) Han, J. H.; Dae Han, C. Bubble Nucleation in Polymeric Liquids 0.2. Theoretical Considerations. *J. Polym. Sci., Part B: Polym. Phys.* **1990**, *28* (5), 743–761.
- (13) Corre, Y. M.; Maazouz, A.; Duchet, J.; Reignier, J. Batch Foaming of Chain Extended Pla with Supercritical CO<sub>2</sub>: Influence of the Rheological Properties and the Process Parameters on the Cellular Structure. *J. Supercrit. Fluids* **2011**, *58* (1), 177–188.
- (14) Di Maio, E.; Iannace, S.; Mensitieri, G.; Nicolais, L. A Predictive Approach Based on the Simha-Somcynsky Free-Volume Theory for the Effect of Dissolved Gas on Viscosity and Glass Transition Temperature of Polymeric Mixtures. *J. Polym. Sci., Part B: Polym. Phys.* **2006**, *44* (13), 1863–1873.
- (15) Kazarian, S. G. Polymers and Supercritical Fluids: Opportunities for Vibrational Spectroscopy. *Macromol. Symp.* **2002**, *184*, 215–228.
- (16) Cotugno, S.; Di Maio, E.; Ciardiello, C.; Iannace, S.; Mensitieri, G.; Nicolais, L. Sorption Thermodynamics and Mutual Diffusivity of Carbon Dioxide in Molten Polycaprolactone. *Ind. Eng. Chem. Res.* **2003**, *42* (19), 4398–4405.
- (17) Pastore Carbone, M. G.; Di Maio, E.; Scherillo, G.; Mensitieri, G.; Iannace, S. Solubility, Mutual Diffusivity, Specific Volume and Interfacial Tension of Molten Pcl/Co<sub>2</sub> Solutions by a Fully Experimental Procedure: Effect of Pressure and Temperature. *J. Supercrit. Fluids* **2012**, *67*, 131–138.
- (18) Markocic, E.; Skerget, M.; Knez, Z. Effect of Temperature and Pressure on the Behavior of Poly(Epsilon-Caprolactone) in the Presence of Supercritical Carbon Dioxide. *Ind. Eng. Chem. Res.* **2013**, *52* (44), 15594–15601.
- (19) Johnston, K. P.; Meredith, J. C.; Harrison, K. L. Spectroscopy: The Fourth Vertex on the Molecular Thermodynamics Tetrahedron. *Fluid Phase Equilib.* **1996**, *116* (1–2), 385–394.
- (20) Nalawade, S. P.; Picchioni, F.; Janssen, L. P. B. M.; Grijpma, D. W.; Feijen, J. Investigation of the Interaction of CO<sub>2</sub> with Poly (L-Lactide), Poly(DL-Lactide) and Poly(E-Caprolactone) Using Ftir Spectroscopy. *J. Appl. Polym. Sci.* **2008**, *109* (5), 3376–3381.
- (21) Meredith, J. C.; Johnston, K. P.; Seminario, J. M.; Kazarian, S. G.; Eckert, C. A. Quantitative Equilibrium Constants between CO<sub>2</sub> and Lewis Bases from Ftir Spectroscopy. *J. Phys. Chem.* **1996**, *100* (26), 10837–10848.
- (22) Kazarian, S. G.; Vincent, M. F.; Bright, F. V.; Liotta, C. L.; Eckert, C. A. Specific Intermolecular Interaction of Carbon Dioxide with Polymers. *J. Am. Chem. Soc.* **1996**, *118* (7), 1729–1736.
- (23) Knauer, O. S.; Pastore Carbone, M. G.; Braeuer, A.; Di Maio, E.; Leipertz, A. Investigation of CO<sub>2</sub> Sorption in Molten Polymers at High Pressures Using Raman Line Imaging. *Polymer* **2013**, *54* (2), 812–818.
- (24) Frisch, M. J.; Headgordon, M.; Pople, J. A. A Direct Mp2 Gradient-Method. *Chem. Phys. Lett.* **1990**, *166* (3), 275–280.
- (25) Frisch, M. J.; Headgordon, M.; Pople, J. A. Semidirect Algorithms for the Mp2 Energy and Gradient. *Chem. Phys. Lett.* **1990**, *166* (3), 281–289.
- (26) Headgordon, M.; Headgordon, T. Analytic Mp2 Frequencies without 5th-Order Storage - Theory and Application to Bifurcated Hydrogen-Bonds in the Water Hexamer. *Chem. Phys. Lett.* **1994**, *220* (1–2), 122–128.
- (27) Allinger, N. L. Conformational Analysis. 130. Mm2. A Hydrocarbon Force Field Utilizing V1 and V2 Torsional Terms. *J. Am. Chem. Soc.* **1977**, *99* (25), 8127–8134.
- (28) Allinger, N. L.; Kok, R. A.; Imam, M. R. Hydrogen Bonding in Mm2. *J. Comput. Chem.* **1988**, *9* (6), 591–595.
- (29) Chang, G.; Guida, W. C.; Still, W. C. An Internal-Coordinate Monte Carlo Method for Searching Conformational Space. *J. Am. Chem. Soc.* **1989**, *111* (12), 4379–4386.
- (30) Morokuma, K.; Kitaura, K. *Molecular Interactions*; Wiley: New York, 1980; Vol. 1.
- (31) Boys, S. F.; Bernardi, F. The Calculation of Small Molecular Interactions by the Differences of Separate Total Energies. Some Procedures with Reduced Errors. *Mol. Phys.* **1970**, *19*, 553–556.
- (32) Wilson, E. B.; Decius, J. C.; Cross, P. C. *Molecular Vibrations*; McGraw-Hill: New York, 1955.
- (33) Scott, A. P.; Radom, L. Harmonic Vibrational Frequencies: An Evaluation of Hartree-Fock, Møller-Plesset, Quadratic Configuration Interaction, Density Functional Theory, and Semiempirical Scale Factors. *J. Phys. Chem.* **1996**, *100* (41), 16502–16513.
- (34) Alecu, I. M.; Zheng, J. J.; Zhao, Y.; Truhlar, D. G. Computational Thermochemistry: Scale Factor Databases and Scale Factors for Vibrational Frequencies Obtained from Electronic Model Chemistries. *J. Chem. Theory Comput.* **2010**, *6* (9), 2872–2887.
- (35) Frisch, M. J.; Trucks, G. W.; Schlegel, H. B.; Scuseria, G. E.; Robb, M. A.; Cheeseman, J. R.; Scalmani, G.; Barone, V.; Mennucci, B.; Petersson, G. A.; et al. *Gaussian 03*, Revision C.02; Gaussian Inc.: Wallingford CT, 2004.
- (36) Jamróz, M. H. *Vibrational Energy Distribution Analysis: Veda 4*; Warsaw, 2010.
- (37) Jamróz, M. H. Vibrational Energy Distribution Analysis (Veda): Scopes and Limitations. *Spectrochim. Acta, Part A* **2013**, *114*, 220–30.
- (38) Howard-Lock, H. E.; Stoicheff, B. P. Raman Intensity Measurements of the Fermi Diad in <sup>12</sup>CO<sub>2</sub> and <sup>13</sup>CO<sub>2</sub>. *J. Mol. Spectrosc.* **1971**, *37*, 321–326.
- (39) Ikeda, T.; Mae, S.; Uchida, T. Effect of Guest-Host Interaction on Raman Spectrum of a CO<sub>2</sub> Clathrate Hydrate Single Crystal. *J. Chem. Phys.* **1998**, *108* (4), 1352–1359.
- (40) Montero, S. Raman Intensities of Fermi Dyads. I. Overtones in Resonance with Non-Degenerate Fundamentals. *J. Chem. Phys.* **1983**, *79*, 4091–4100.
- (41) Uchida, T.; Takagi, A.; Mae, S.; Kawabata, J. Dissolution Mechanisms of CO<sub>2</sub> Molecules in Water Containing CO<sub>2</sub> Hydrates. *Energy Convers. Manage.* **1997**, *38*, S307–S312.
- (42) Nakahara, J.; Shigesato, Y.; Higashi, A.; Hondoh, T.; Langway, C. C., Jr Raman Spectra of Natural Clathrates in Deep Ice Cores. *Philos. Mag. B* **1988**, *57* (3), 421–430.
- (43) Cahill, J. E.; Leroi, G. E. Raman Spectra of Solid CO<sub>2</sub>, N<sub>2</sub>O, N<sub>2</sub>, and Co. *J. Chem. Phys.* **1969**, *51*, 1324–1332.
- (44) Rajta, I.; Szilasi, S. Z.; Budai, J.; Toth, Z.; Petrik, P.; Baradacs, E. Refractive Index Depth Profile in Pmma Due to Proton Irradiation. *Nucl. Instrum. Methods Phys. Res., Sect. B* **2007**, *260* (1), 400–404.
- (45) Sloan, E. D., Jr. *Clathrate Hydrates of Natural Gases*; Marcel Dekker Inc.: New York, 1990.
- (46) Xia, Z.; Trexler, M.; Wu, F.; Jean, Y. C.; Van Horn, J. D. Free-Volume Hole Relaxation in Molecularly Oriented Glassy Polymers. *Physical review. E, Statistical, nonlinear, and soft matter physics* **2014**, *89* (2), 022603.
- (47) Ward, S. A.; Pethrick, R. A. Positron Annihilation Lifetime Spectroscopy and Diffusion Studies of Large Molecule Penetrants into a Polyester. *Polym. Eng. Sci.* **2012**, *52* (9), 1978–1984.
- (48) Ward, S. A.; Pethrick, R. A. Positron Annihilation Lifetime Spectroscopy and Diffusion Studies of Large Molecule Penetrants into Alkyd Resins. *Prog. Org. Coat.* **2012**, *75* (4), 509–526.
- (49) Pethrick, R. A. Positron Annihilation - a Probe for Nanoscale Voids and Free Volume? *Prog. Polym. Sci.* **1997**, *22* (1), 1–47.
- (50) Ikeda-Fukazawa, T.; Kita, D.; Nagashima, K. Raman Spectroscopic Study of CO<sub>2</sub> Sorption Process in Poly Methyl Methacrylate. *J. Polym. Sci., Part B: Polym. Phys.* **2008**, *46* (8), 831–842.
- (51) Chalmers, J. M.; Griffiths, P. R. *Handbook of Vibrational Spectroscopy*; Wiley: Chichester, U.K., 2002; Vol. 1.
- (52) Pastore Carbone, M. G.; Di Maio, E.; Iannace, S.; Mensitieri, G. Simultaneous Experimental Evaluation of Solubility, Diffusivity, Interfacial Tension and Specific Volume of Polymer/Gas Solutions. *Polym. Test.* **2011**, *30* (3), 303–309.
- (53) Crank, J. *The Mathematics of Diffusion*, 2nd ed.; Clarendon Press: Oxford, 1975.
- (54) Panayiotou, C.; Pantoula, M.; Stefanis, E.; Tsvintzelis, I.; Economou, I. G. Nonrandom Hydrogen-Bonding Model of Fluids and Their Mixtures. I. Pure Fluids. *Ind. Eng. Chem. Res.* **2004**, *43* (20), 6592–6606.

- (55) Panayiotou, C.; Tsivintzelis, I.; Economou, I. G. Nonrandom Hydrogen-Bonding Model of Fluids and Their Mixtures. 2. Multi-component Mixtures. *Ind. Eng. Chem. Res.* **2007**, *46* (8), 2628–2636.
- (56) Jarmelo, S.; Marques, D. A.; Simões, P. N.; Carvalho, R. A.; Batista, C. M.; Araujo-Andrade, C.; Gil, M. H.; Fausto, R. Experimental (Ir/Raman and <sup>1</sup>h/<sup>13</sup>C Nmr) and Theoretical (Dft) Studies of the Preferential Conformations Adopted by L-Lactic Acid Oligomers and Poly(L-Lactic Acid) Homopolymer. *J. Phys. Chem. B* **2012**, *116* (1), 9–21.
- (57) Honda, K.; Furukawa, Y.; Nishide, H. Dft Oligomer Approach to Vibrational Spectra of Poly(P-Phenylenevinylene). *Vib. Spectrosc.* **2006**, *40*, 149–154.
- (58) Milani, A.; Tommasini, M.; Castiglioni, C.; Zerbi, G.; Radice, S.; Canil, G.; Toniolo, P.; Triulzi, F.; Colaianna, P. Spectroscopic Studies and First-Principles Modelling of 2,2,4-Trifluoro-5-Trifluoromethoxy-1,3-Dioxole (Ttd) and Ttd-Tfe Copolymers (Hyflon Ad). *Polymer* **2008**, *49*, 1812–1822.
- (59) Radice, S.; Canil, G.; Toniolo, P.; Guarda, P. A.; Petricci, S.; Milani, A.; Tommasini, M.; Castiglioni, G.; Zerbi, G. Infrared Intensity Studies in Fluorinated Macromolecules. *Macromol. Symp.* **2008**, *265*, 218–224.
- (60) Kamiya, M.; Tsuneda, T.; Hirao, K. A Density Functional Study of Van Der Waals Interactions. *J. Chem. Phys.* **2002**, *117* (13), 6010–6015.
- (61) Kohn, W.; Meir, Y.; Makarov, D. E. Van Der Waals Energies in Density Functional Theory. *Phys. Rev. Lett.* **1998**, *80* (19), 4153–4156.
- (62) Wu, X.; Vargas, M. C.; Nayak, S.; Lotrich, V.; Scoles, G. Towards Extending the Applicability of Density Functional Theory to Weakly Bound Systems. *J. Chem. Phys.* **2001**, *115* (19), 8748–8757.
- (63) Kilic, S.; Michalik, S.; Wang, Y.; Johnson, J. K.; Enick, R. M.; Beckman, E. J. Effect of Grafted Lewis Base Groups on the Phase Behavior of Model Poly(Dimethyl Siloxanes) in Co<sub>2</sub>. *Ind. Eng. Chem. Res.* **2003**, *42* (25), 6415–6424.
- (64) Kilic, S.; Michalik, S.; Wang, Y.; Johnson, J. K.; Enick, R. M.; Beckman, E. J. Phase Behavior of Oxygen-Containing Polymers in Co<sub>2</sub>. *Macromolecules* **2007**, *40* (4), 1332–1341.
- (65) Oakes, R. E.; Beattie, J. R.; Moss, B. W.; Bell, S. E. J. Conformations, Vibrational Frequencies and Raman Intensities of Short-Chain Fatty Acid Methyl Esters Using Dft with 6-31g(D) and Sadlej Pvtz Basis Sets. *J. Mol. Struct.: THEOCHEM* **2002**, *586*, 91–110.
- (66) Oakes, R. E.; Beattie, J. R.; Moss, B. W.; Bell, S. E. J. Dft Studies of Long-Chain Fames: Theoretical Justification for Determining Chain Length and Unsaturation from Experimental Raman Spectra. *J. Mol. Struct.: THEOCHEM* **2003**, *626*, 27–45.
- (67) Kister, G.; Cassanas, G.; Bergounhon, M.; Hoarau, D.; Vert, M. Structural Characterization and Hydrolytic Degradation of Solid Copolymers of D,L-Lactide-Co-E-Caprolactone by Raman Spectroscopy. *Polymer* **2000**, *41* (3), 925–932.
- (68) Nelson, M. R.; Borkman, R. F. Ab Initio Calculations on Co<sub>2</sub> Binding to Carbonyl Groups. *J. Phys. Chem. A* **1998**, *102* (40), 7860–7863.
- (69) Jamroz, M. H.; Dobrowolski, J. C.; Bajdor, K.; Borowiak, M. A. Ab-Initio Study of the Nu(Co<sub>2</sub>) Mode in Eda Complexes. *J. Mol. Struct.* **1995**, *349*, 9–12.
- (70) Wang, J.; Wang, M.; Hao, J.; Fujita, S.; Arai, M.; Wu, Z.; Zhao, F. Theoretical Study on Interaction between Co<sub>2</sub> and Carbonyl Compounds: Influence of Co<sub>2</sub> on Infrared Spectroscopy and Activity of C=O. *J. Supercrit. Fluids* **2010**, *54*, 9–15.
- (71) Chen, J. G.; Liu, X.; Liu, Z. W.; Hu, D. D.; Zhang, C. J.; Xue, D.; Xiao, J. L.; Liu, Z. T. Intermolecular-Interaction-Dominated Solvation Behaviors of Liquid Monomers and Polymers in Gaseous and Supercritical Carbon Dioxide. *Macromolecules* **2012**, *45* (11), 4907–4919.
- (72) Raveendran, P.; Wallen, S. L. Cooperative C-H...O Hydrogen Bonding in Co<sub>2</sub>-Lewis Base Complexes: Implications for Solvation in Supercritical Co<sub>2</sub>. *J. Am. Chem. Soc.* **2002**, *124* (42), 12590–12599.
- (73) Blatchford, M. A.; Raveendran, P.; Wallen, S. L. Raman Spectroscopic Evidence for Cooperative C-H...O Interactions in the Acetaldehyde-Co<sub>2</sub> Complex. *J. Am. Chem. Soc.* **2002**, *124*, 14818–14819.
- (74) Vargas, R.; Garza, J.; Dixon, D. A.; Hay, B. P. How Strong Is the C<sub>a</sub>-H...O=C Hydrogen Bond? *J. Am. Chem. Soc.* **2000**, *122* (19), 4750–4755.
- (75) Hobza, P.; Spirko, V.; Havlas, Z.; Buchhold, K.; Reimann, B.; Barth, H. D.; Brutschy, B. Anti-Hydrogen Bond between Chloroform and Fluorobenzene. *Chem. Phys. Lett.* **1999**, *299* (2), 180–186.
- (76) Hobza, P.; Spirko, V.; Selzle, H. L.; Schlag, E. W. Anti-Hydrogen Bond in the Benzene Dimer and Other Carbon Proton Donor Complexes. *J. Phys. Chem. A* **1998**, *102* (15), 2501–2504.
- (77) Vargas, R.; Garza, J.; Dixon, D. A.; Hay, B. P. Conformational Analysis of N,N,N',N'-Tetramethylsuccinamide: The Role of C-H...O Hydrogen Bonds. *J. Phys. Chem. A* **2000**, *104* (21), 5115–5121.
- (78) Scheiner, S.; Gu, Y.; Kar, T. Evaluation of the H-Bonding Properties of C-H...O Interactions Based Upon Nmr Spectra. *J. Mol. Struct.: THEOCHEM* **2000**, *500*, 441–452.
- (79) Steiner, T. Unrolling the Hydrogen Bond Properties of C-H Center Dot Center Dot Center Dot O Interactions. *Chem. Commun.* **1997**, *8*, 727–734.
- (80) Hobza, P.; Havlas, Z. Blue-Shifting Hydrogen Bonds. *Chem. Rev.* **2000**, *100* (11), 4253–4264.
- (81) Pedireddi, V. R.; Chatterjee, S.; Ranganathan, A.; Rao, C. N. R. Noncovalent Synthesis of Layered and Channel Structures Involving Sulfur-Mediated Hydrogen Bonds. *J. Am. Chem. Soc.* **1997**, *119* (44), 10867–10868.
- (82) Steiner, T.; Saenger, W. Weak Polar Host-Guest Interactions Stabilizing a Molecular Cluster in a Cyclodextrin Cavity - C-H-O and C-H-X Contacts in Beta-Cyclodextrin-but-2-Yne-L,4-Diol Heptahydrate. *J. Chem. Soc., Chem. Commun.* **1995**, *20*, 2087–2088.
- (83) Houk, K. N.; Menzer, S.; Newton, S. P.; Raymo, F. M.; Stoddart, J. F.; Williams, D. J. Molecular Meccano. 47. [C-H - O] Interactions as a Control Element in Supramolecular Complexes: Experimental and Theoretical Evaluation of Receptor Affinities for the Binding of Bipyridinium-Based Guests by Catenated Hosts. *J. Am. Chem. Soc.* **1999**, *121* (7), 1479–1487.
- (84) Shimon, L. J. W.; Vaida, M.; Addadi, L.; Lahav, M.; Leiserowitz, L. Molecular Recognition at the Solid-Solution Interface - a Relay Mechanism for the Effect of Solvent on Crystal-Growth and Dissolution. *J. Am. Chem. Soc.* **1990**, *112* (17), 6215–6220.
- (85) Keegstra, E. M. D.; Spek, A. L.; Zwikker, J. W.; Jennekens, L. W. The Crystal-Structure of 2-Methoxy-1,4-Benzoquinone - Molecular Recognition Involving Intermolecular Dipole-Dipole- and C-H...O Hydrogen-Bond Interactions. *J. Chem. Soc., Chem. Commun.* **1994**, *14*, 1633–1634.
- (86) Leonard, G. A.; Mcauleyhecht, K.; Brown, T.; Hunter, W. N. Do C-H...O Hydrogen-Bonds Contribute to the Stability of Nucleic-Acid Base-Pairs. *Acta Crystallogr., Sect. D: Biol. Crystallogr.* **1995**, *51*, 136–139.
- (87) Musah, R. A.; Jensen, G. M.; Rosenfeld, R. J.; McRee, D. E.; Goodin, D. B.; Bunte, S. W. Variation in Strength of an Unconventional C-H to O Hydrogen Bond in an Engineered Protein Cavity. *J. Am. Chem. Soc.* **1997**, *119* (38), 9083–9084.
- (88) Desiraju, G. R. The C-H...O Hydrogen Bond: Structural Implications and Supramolecular Design. *Acc. Chem. Res.* **1996**, *29* (9), 441–449.
- (89) Mulliken, R. S. Electronic Population Analysis on Lcao-Mo Molecular Wave Functions. I. *J. Chem. Phys.* **1955**, *23* (10), 1833–1840.
- (90) Musto, P.; Galizia, M.; Pannico, M.; Scherillo, G.; Mensitieri, G. Time-Resolved Fourier Transform Infrared Spectroscopy, Gravimetry, and Thermodynamic Modeling for a Molecular Level Description of Water Sorption in Poly(E-Caprolactone). *J. Phys. Chem. B* **2014**, *118* (26), 7414–29.
- (91) Kirkwood, J. On the Theory of Dielectric Polarization. *J. Chem. Phys.* **1936**, *4*, 592–601.
- (92) Bauer, E.; Magat, M. Sur La Déformation Des Molécules En Phase Condensée Et La « Liaison Hydrogène ». *J. Phys. Radium* **1938**, *9* (8), 319–330.

(93) May, E. F.; Moldover, M. R.; Schmidt, J. W. The Dielectric Permittivity of Saturated Liquid Carbon Dioxide and Propane Measured Using Cross Capacitors. *Int. J. Thermophys.* **2005**, *26* (3), 563–576.

(94) Wong, M. W.; Wiberg, K. B.; Frisch, M. Hartree–Fock Second Derivatives and Electric Field Properties in a Solvent Reaction Field: Theory and Application. *J. Chem. Phys.* **1991**, *95*, 8991–8998.